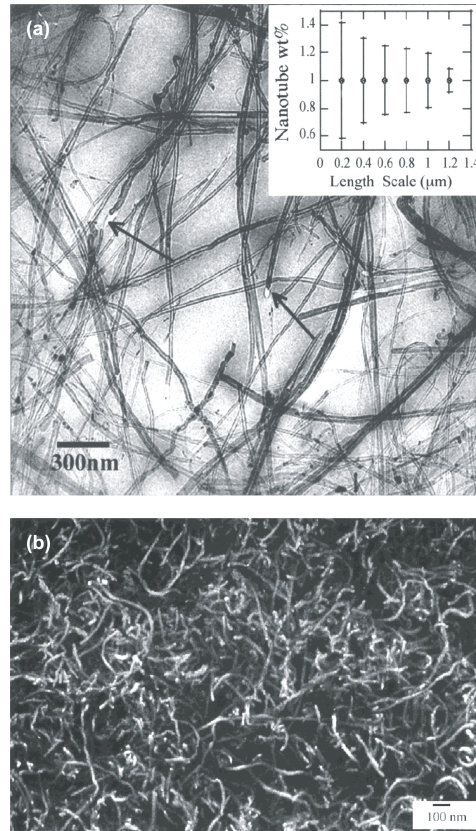


# **CHAPTER 3: NANOTUBE WAVINESS AND THE EFFECTIVE MODULUS OF NANOTUBE-REINFORCED POLYMERS**

## **Introduction**

In order to increase our understanding of the mechanical behavior of nanotube-reinforced polymers, it is useful to develop models of the effective properties of these materials, enabling detailed study of the material system. One means to accomplish this is the extension of traditional micromechanics and composite models to address specific features characteristic of these materials. As an example, consider the high-magnification electron microscopy images of nanotubes embedded in a polymer matrix shown in Figure 18. In the images the nanotubes appear to be wavy (not straight), a feature not typically associated with traditional fiber reinforced composites. Note that this waviness is inherently distinct from the uniform and controlled waviness of the yarns in traditional textile composites. While one might expect that this waviness will reduce the effectiveness of these inclusions for purposes of modulus enhancement, modeling of this reduction will lead to more accurate quantitative models of the mechanical behavior of these materials.



**Figure 18. Micrographs showing the waviness of nanotubes embedded in polymers. (a) TEM image of 1 wt% MWNTs in polystyrene (Qian, Dickey et al. 2000). (b) SEM image of 50 wt% MWNTs in poly(vinyl alcohol). (Shaffer and Windle 1999)**

Motivated by such observations, the model presented in this chapter has been developed to analyze how this waviness impacts the effective moduli of NRPs. This is accomplished via a hybrid finite element-micromechanical model that determines the *effective reinforcing modulus* (ERM) of a wavy embedded nanotube. As demonstrated later in this chapter, the effective reinforcing modulus is then used within a multiphase

micromechanics model to predict the effective modulus of a polymer reinforced with a distribution of wavy nanotubes. We found that even slight nanotube curvature significantly reduces the effective reinforcement in comparison to models assuming straight nanotubes. Using experimental data, we demonstrate that nanotube waviness can significantly limit the property enhancement of the NRP. Thus nanotube waviness may be one reason why the modulus enhancements for NRP systems measured to date, while significant, have been much less than would be anticipated using standard micromechanics models.

At the moment it is impossible to differentiate the impact of nanotube waviness from competing reinforcement-limiting mechanisms such as a weak NT-polymer interface, poor dispersion, and NT degradation in experimental data. Nevertheless, our results provide a clear picture of how moderate waviness can hinder the effectiveness of NTs as structural reinforcement. While the work reported here is an application of a micromechanics method to a nanostructured material, the integration of atomic scale modeling could readily be adapted into such an analysis. In the future a fusion of true nanoscale and microscale modeling will provide even more insight, and quantitatively accurate predictions, of this material behavior.

Next we will describe the models that were developed to determine the effective reinforcing moduli of an embedded wavy nanotube. We will then show how the results of this finite element modeling can be incorporated into micromechanics

techniques to determine the effective modulus of an NRP with randomly orientated, wavy nanotubes. We will then present results that demonstrate how the waviness of the nanotube limits the effective reinforcement that the inclusion provides the host polymer material. This reduced reinforcement results in effective moduli predictions that are significantly lower than those derived assuming straight nanotube inclusions. In all cases these reduced moduli values are in closer agreement with experimental data published in the literature, although currently it is impossible to separate the effects of NT waviness from other reinforcement-limiting mechanisms influencing the effective material behavior. We will also briefly describe an alternative (albeit related) model that has been developed and addresses the impact of NT waviness via the numerical calculation of the dilute strain concentration tensor (Bradshaw, Fisher et al. 2002). At the end of the chapter we will summarize the results of these models and discuss how these results may influence future developments in the area of nanotube-reinforced polymers.

## **The Model**

Based on the discussion of the last section, we are interested in using micromechanical techniques to study the effective elastic moduli of nanotube-reinforced polymers. The basis of the current model is to determine the *effective*

reinforcing modulus (ERM) of the wavy embedded nanotube; that is, a *representative* value denoted  $E_{ERM}$  that accounts for the reduction in reinforcement provided by the wavy nanotube in comparison to the reinforcement provided by a straight NT (of modulus  $E_{NT}$ ).<sup>1</sup> Thus while the nanotube modulus  $E_{NT}$  is a material property, the effective reinforcing modulus  $E_{ERM}$  ( $E_{ERM} \leq E_{NT}$ ) is a material parameter that is a function of the geometry of the wavy nanotube and other variables (as discussed later in this chapter). This effective modulus is then available for use in standard micromechanical models in lieu of the true (actual) nanotube modulus. While such a procedure can be applied in general to any class of curved and wavy inclusions, embedded nanotubes and NRPs are the focus of the present discussion.

In this regard, we note the results of several researchers who found that continuum models provide useful insight into nanotube behavior, despite the discrete nature of their atomic structure (Ruoff and Lorents 1995; Yakobson and Smalley 1997).<sup>2</sup> To simplify the geometry we will treat the nanotube as a solid element of circular cross-sectional area, which implicitly introduces two simplifications into the analysis. First, treating the inclusion as a solid cylinder neglects the hollow nature of

---

<sup>1</sup> This effective reinforcing modulus  $E_{ERM}$  is identical to what we have called the wavy nanotube modulus ( $E_{wavy}$ ) in previous work (Fisher, Bradshaw et al. 2002a).

<sup>2</sup> Others have found a large number of atomic layers was necessary to justify the treatment of the nanotube as a continuum (Govindjee and Sackman 1999). However, for the purposes of moduli predictions we believe that a continuum assumption is an acceptable simplification. Other mechanical behavior, such as crack propagation and fracture, will undoubtedly be more dependent on atomic structure and may be especially ill-suited for such an assumption.

the nanotubes.<sup>3</sup> Second, by modeling the nanotube as a continuum we are disregarding the specific form of the nanotube (SWNT, MWNT, or bundle) and neglecting any possible relative motion between individual shells or tubes in a MWNT and an NT bundle, respectively. Each of these assumptions suggests that  $E_{ERM}$  as calculated here is an “upper bound” for the given model, in that accounting for the hollow nature of the NTs or modeling relative sliding of the tubes or shells would further reduce the effective stiffness of a wavy nanotube. Thus nanotube waviness may be even more significant than the results presented in this work would indicate. While this approach will highlight the impact of nanotube waviness on the effective modulus of an NRP, a more rigorous analysis that accounts for the discrete nature of the nanotube and the atomic interaction between the nanotube and polymer is warranted and will be the subject of future work.

In addition to the continuum assumption, several other simplifications are invoked throughout this work to aid in the interpretation of the results. The individual phase materials are modeled as linear elastic and isotropic, and perfect bonding between the phases is assumed. The waviness of a nanotube of diameter  $d$  will be introduced by prescribing an embedded NT shape of the form  $y = a \cos(2\pi z / \lambda)$ , where  $\lambda$  is the sinusoidal wavelength and  $z$  is the fiber axial direction (see Figure 21

---

<sup>3</sup> It is also well established that in many cases the cross-section of the nanotubes is not circular but is typically distorted due to van der Waals interactions between the shells (or tubes). However, for our current investigation the effect of this slight distortion in cross-sectional shape is negligible.

on page 63). Unless otherwise noted, Poisson ratios of 0.30 were assumed for all phases in the simulations; this value is representative of a wide range of polymer materials, and is consistent with the range of values estimated for carbon nanotubes. This assumption will be discussed in more detail later in this chapter.

We will first present our initial efforts to develop an analytical model describing the extension of a wavy NT in response to an applied axial load. While it was useful to consider such an initial model, we found that its utility was greatly limited due to the inability to accurately capture the influence of the surrounding matrix on the response of the wavy nanotube. This led us to study the problem via the finite element analysis, where the constraint of the surrounding matrix can now be considered. Following this, the formulation of the Mori-Tanaka method for a multiphase composite with randomly aligned cylindrical inclusions in two- and three-dimensional space will be presented. Finally, we will present a multiphase composite approach where the nanotubes are modeled as a finite number of discrete inclusion phases with distinct effective moduli based on their embedded waviness.

### ***Analytical solution for an isolated wavy nanotube***

A critical component of the problem at hand is to model the mechanical response of an *embedded* wavy nanotube, due to an applied axial load  $P$ , as a function of waviness. As a first approximation it is insightful to consider the analytical solution

for the effective stiffness of a *free-standing* wavy rod subject to axial load. We will later show that such a model is only useful when the modulus of the *straight* nanotube  $E_{NT}$  is much larger than the modulus of the matrix  $E_{matrix}$ . When this criterion is not satisfied (i.e.  $E_{NT}/E_{matrix} < 1000$ ), a finite element analysis is necessary to account for the lateral constraint that the surrounding matrix provides the embedded nanotube. For completeness, we briefly describe the analytical solution for a free-standing wavy rod below.

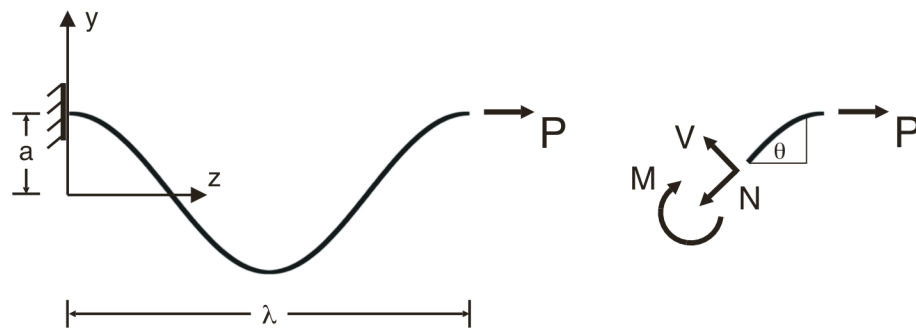


**Figure 19. Schematic of the analytical solution for a free-standing wavy fiber.**

Consider the sinusoidal wavy rod of solid cross-section shown in Figure 19. Assuming linear elastic material behavior and small displacements, Castigliano's theorem states that the displacements due to an applied load  $P$ , in the direction of  $P$ , are given by  $\Delta_P = \partial U / \partial P$ , where  $U$  is the total elastic strain energy of the system (Boresi, Schmidt et al. 1993). Given the sinusoidal geometry of the free-standing

nanotube, one can determine the internal axial ( $N$ ) and shear ( $V$ ) forces and the internal moment ( $M$ ) within the rod as a function of  $z$ :

$$\begin{aligned}
 N(z) &= P \cos(\varphi) = \frac{P}{\sqrt{1 + \frac{4a^2}{\varphi^2} \sin^2\left(\frac{2\varphi z}{\varphi}\right)}}, \\
 V(z) &= P \sin(\varphi) = \frac{\frac{2a}{\varphi} P \sin\left(\frac{2\varphi z}{\varphi}\right)}{\sqrt{1 + \frac{4a^2}{\varphi^2} \sin^2\left(\frac{2\varphi z}{\varphi}\right)}}, \\
 M(z) &= P[a \varphi y(z)] = Pa \frac{\varphi}{\varphi} \cos\left(\frac{2\varphi z}{\varphi}\right).
 \end{aligned} \tag{3}$$

The total end displacement  $\varphi_P$  of the rod is then the sum of the components due to each of these terms, integrated over one wavelength  $\varphi$  of the sinusoidal rod,

$$\varphi_P = \varphi_N + \varphi_V + \varphi_M = \varphi \left[ \frac{N}{EA} \frac{\partial N}{\partial P} ds + \frac{kV}{GA} \frac{\partial V}{\partial P} ds + \frac{M}{EI} \frac{\partial M}{\partial P} ds \right], \tag{4}$$

where  $\varphi_N$ ,  $\varphi_V$ , and  $\varphi_M$  are the contributions due to the internal axial and shear forces, and the internal moment, respectively, and  $ds$  is an increment of arc length. In this expression  $k$  is the correction factor for the shear strain energy (equal to 1.33 for a solid circular cross section (Boresi, Schmidt et al. 1993)),  $G$  is the shear modulus, and

$A$  and  $I$  are the cross sectional area and the moment of inertia for a circular cross section. By substituting (3) into (4) and with further simplification, the components of the axial displacement of the free-standing wavy rod are

$$\Delta_N = \frac{P}{AE} \int_0^L \frac{1}{\sqrt{1 + \frac{4a^2}{L^2} \sin^2 \frac{2\pi z}{L}}} dz, \quad (5)$$

$$\Delta_V = \frac{4a^2 \pi^2 kP}{AG \pi^2} \int_0^L \frac{\sin^2 \frac{2\pi z}{L}}{\sqrt{1 + \frac{4a^2}{L^2} \sin^2 \frac{2\pi z}{L}}} dz, \quad (6)$$

$$\Delta_M = \frac{a^2 P}{IE} \int_0^L \cos \frac{2\pi z}{L} \sqrt{1 + \frac{4a^2}{L^2} \sin^2 \frac{2\pi z}{L}} dz. \quad (7)$$

Given these displacement components, the total displacement of the end of the rod is given via (4). Note that in the limit of a straight rod ( $a=0$ ), the above expression yields the standard expression for the extension of straight rod under uniaxial tension,

$$\Delta = \frac{PL}{AE}.$$

We now define the *effective* reinforcing modulus of the free-standing wavy rod as the ratio of the applied stress to the resulting strain, such that

$$E_{\text{free}} = \frac{\sigma}{\epsilon} = \frac{P/A}{\epsilon_p/L} = \frac{PL}{A\epsilon_p}. \quad (8)$$

This expression, normalized with respect to the true modulus, is plotted versus waviness  $w$  (defined as the ratio of sinusoidal amplitude to wavelength  $a/\lambda$ ) in Figure 20 for  $\lambda/d=100$ . Also shown in Figure 20 are the results of an analogous finite element model (described later in the chapter), which indicate excellent agreement between the two solutions. The slight difference between the solutions is attributed to the imposed displacement boundary conditions in the finite element model, which prevent vertical displacement of the rod at  $z=0$ . As expected, the effective modulus quickly falls off with increasing waviness, such that for even very minimal values of waviness the effective stiffness is negligible (i.e. for  $w=a/\lambda=0.01$ , the effective stiffness is less than 5% of the true modulus).

We found that this analytical solution is limited in the present analysis because it does not reflect the physical nature of the constraint imposed by the surrounding matrix. Specifically, comparison of this analytical solution with our finite element results for an embedded wavy nanotube (described later) show that the free-standing solution severely underestimates the effective stiffness of embedded wavy inclusions. As demonstrated in Figure 20, if one were to use the analytical model in (8), it would be possible for the effective reinforcing modulus of a stiff inclusion to be less than the

matrix modulus. As such the wavy nanotube would *decrease* the effective modulus of the NRP, a result that is clearly not realistic.

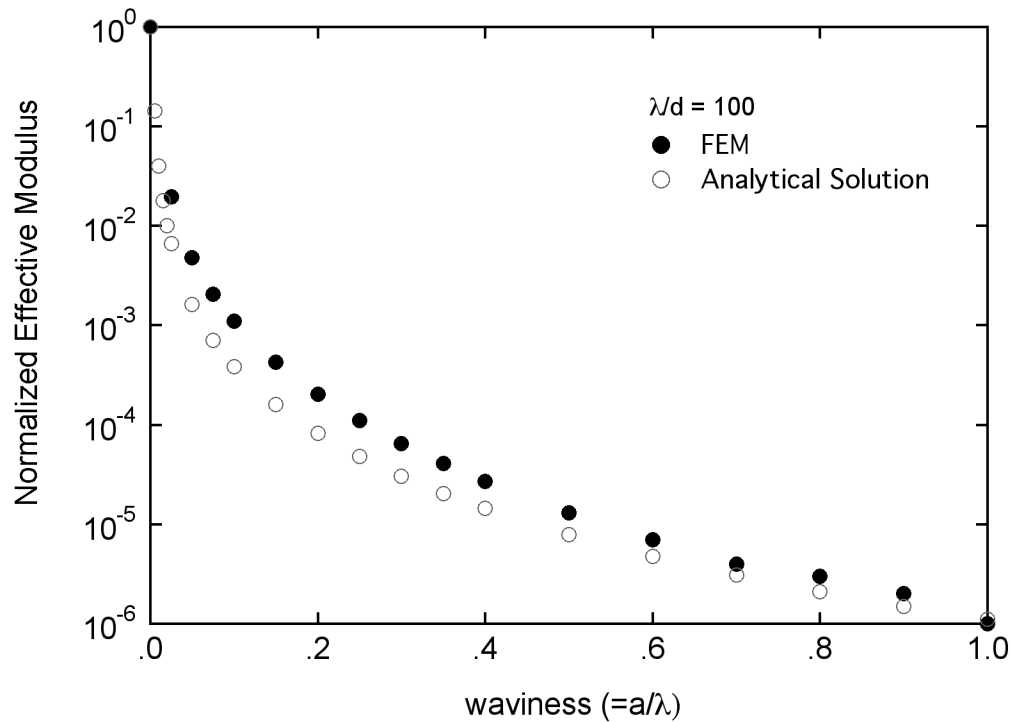


**Figure 20. Comparison of finite element and analytical solutions for the effective modulus of a free-standing wavy rod.**

Attempts to adapt this analytical solution for the case of the embedded wavy inclusions were not successful, primarily because of the difficulty in accounting for the additional constraint of the surrounding matrix. For example, the Rule of Mixtures approximation is ill-suited for this analysis because the volume fraction of the free-standing nanotube is not well defined. This difficulty is eliminated in our finite

element model of the effective reinforcing modulus, which is discussed in the next section and will be the focus of the remainder of this chapter.

### ***Finite element model for the effective reinforcing modulus***

To determine the effective reinforcing moduli  $E_{ERM}$  of an embedded wavy nanotube, ANSYS<sup>TM</sup> was used to create and analyze a three dimensional finite element model of a single, infinitely long wavy nanotube of diameter  $d$  perfectly bonded within a matrix material. For axial loading the problem is symmetric about the  $x=0$  and  $z=n\pi/2$  (where  $n$  is an integer) planes; thus the quarter-symmetric unit cell shown in Figure 21 is used for the analysis. The size of the cell was chosen such that the effective cell response is independent of additional matrix material (this proof is provided later in this chapter). A more complete description of the finite element modeling used here has been described in the literature (Bradshaw, Fisher et al. 2002).

For the finite element simulations symmetry conditions  $u_x=0$  and  $u_z=0$  were prescribed on the  $x=0$  and  $z=0$  planes, respectively. The model was constrained in the  $y$  direction at a single point to prevent free body translation, and an infinitesimally small axial displacement,  $\Delta$ , prescribed to all nodes on the plane  $z=\pi/2$ . The effective modulus of the finite element cell is defined as

$$E_{cell}^{FEA} = \frac{F_{tot} \Delta}{2 A \Delta}, \quad (9)$$

where  $F_{tot}$  is the sum of all nodal resultant forces on the displaced plane and  $A$  is the cross-sectional area of the cell.

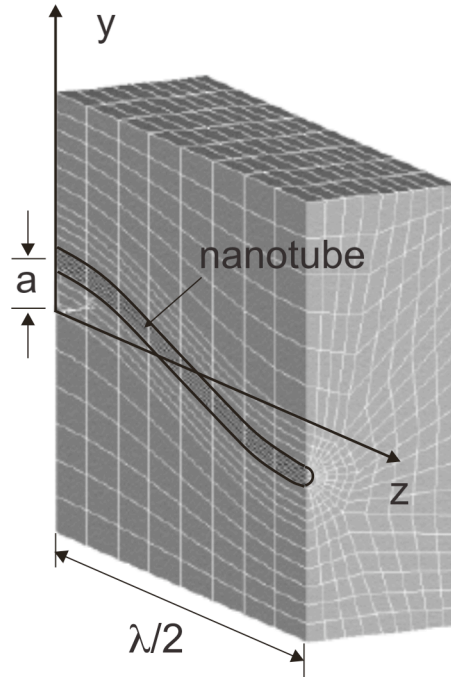


**Figure 21. Finite element cell model of an embedded wavy nanotube. For the model shown,  $w=a/\lambda=0.1$  and  $\lambda/d=35$ .**

In order to extract the effective reinforcing moduli of the *embedded* wavy inclusion (as it exists in the matrix) from (9), we propose a parallel model of the effective cell response, independent of the previous analysis,

$$E_{cell}^{parallel} = c_{NT} E_{ERM} + (1 - c_{NT}) E_{matrix}, \quad (10)$$

where  $c_{NT}$  is the nanotube volume fraction within the finite element cell and  $E_{matrix}$  is the matrix modulus. From (9) and (10),  $E_{ERM}$  of the embedded inclusion can be calculated as

$$E_{ERM} = \frac{E_{cell}^{FEA} (1 - c_{NT}) E_{matrix}}{c_{NT}}. \quad (11)$$

Thus  $E_{ERM}$  represents the modulus of a straight inclusion that, under identical loading conditions, would yield the same effective finite element cell response as that obtained with the wavy inclusion.

This finite element solution is a powerful tool to model the effective response of embedded wavy inclusions. While at first glance the number of parameters affecting  $E_{cell}^{FEA}$  (and hence  $E_{ERM}$ ) appears quite large, we will show later in this chapter that for the model described above, and an additional assumption that the Poisson ratios of the phases are equal,  $E_{ERM}$  will only be dependent on three parameters: the waviness ratio ( $w=a/\lambda$ ) and wavelength ratio ( $\lambda/d$ ) of the nanotube and the ratio of the phase moduli ( $E_{ratio}=E_{NT}/E_{matrix}$ ). A systematic analysis of the impact of these parameters on  $E_{ERM}$  was undertaken and the key results will be presented later in this chapter. The benefit of such an analysis is that it allows inclusion waviness to be integrated into traditional micromechanics techniques by simply modeling the wavy

inclusions as straight inclusions with a reduced reinforcing modulus  $E_{ERM}$  determined via finite element modeling.

### Analytical solution for $E_{cell}$

After the development of the finite element model presented above, it was brought to our attention that in certain circumstances the value for  $E_{cell}$  can be approximated using analytical expressions developed for the analysis of flexible fiber composites (Chou and Takahashi 1987; Kuo, Takahashi et al. 1988). Specifically, the effective Young's modulus for a composite with isophase sinusoidal fibers can be written as

$$E_x^* = \frac{(1+c)^{3/2}}{\frac{1}{E_f} + \frac{c}{2} S_{11} + \frac{3}{2} c (1+c)^{3/2} S_{22} + \frac{c}{2} (2S_{12} + S_{66})} \quad (12)$$

where  $c = (2a/\lambda)^2$  and  $S_{ij}$  are the elastic compliance terms which relate longitudinal (L) and transverse (T) stresses and strains of the *unidirectional* straight fiber composite via

$$\begin{bmatrix} \epsilon_L \\ \epsilon_T \\ \epsilon_{LT} \end{bmatrix} = \begin{bmatrix} S_{11} & S_{12} & 0 \\ S_{12} & S_{22} & 0 \\ 0 & 0 & S_{66} \end{bmatrix} \begin{bmatrix} \sigma_L \\ \sigma_T \\ \sigma_{LT} \end{bmatrix} \quad (13)$$

The key aspect of the analysis is that a sufficiently small volume fraction of straight inclusion must be assumed in (13), such that the resulting elastic compliance terms approximate the dilute solution response modeled in the finite element analysis. Similar to the analysis using the finite element method, these terms will converge for a sufficiently small volume fraction of inclusions, which we found to be on the order of 0.01%.

Similar to the Analytical Long Wavelength (ALW) model presented later in this chapter, the analytical expressions above can be used to approximate  $E_{\text{cell}}$  from the finite element analysis when the wavelength ratio  $\lambda/d$  is sufficiently large for the case of a given waviness ratio  $a/\lambda$ . When  $a/\lambda$  is too large for a given wavelength ratio, the analytical solution underestimates the value of  $E_{\text{cell}}$  determined from the finite element analysis. For consistency, in the current work the values for  $E_{\text{cell}}$  were taken directly from the finite element simulations.

### **Convergence of $E_{\text{ERM}}$ for a sufficiently large matrix**

In order to eliminate the size of the finite element model as a parameter in the analysis, it is necessary to show that  $E_{\text{ERM}}$  converges for a sufficiently large matrix. To accomplish this we consider a finite element cell of an embedded wavy nanotube (see Figure 21), where for simplicity we redefine the length of the cell as  $L$  (to eliminate carrying a factor of two in our analysis below). We assume that the matrix

boundary at the top and bottom of the cells is sufficiently far from the nanotube such that fields at these boundaries are undisturbed by the presence of the nanotube, and denote the volumes of the NT, matrix, and total cell as  $V_{NT}$ ,  $V_{matrix}$ , and  $V$ , respectively. Note that a respective area is given as  $A=V/L$ . We apply an infinitesimally small uniform strain  $\epsilon_z$  in the fiber axial direction and measure the total resultant force  $F_{tot}$  necessary to cause this strain. From (10) and (11) we can write the effective reinforcing modulus for this particular finite element cell as

$$E_{ERM_1} = \frac{\frac{F_{tot} L}{V \epsilon_z} \left[ \frac{V_{mat}}{V} E_{mat} \right]}{\frac{V_{NT}}{V}} = \frac{F_{tot} L}{V_{NT} \epsilon_z} \left[ \frac{V_{mat}}{V_{NT}} E_{mat} \right]. \quad (14)$$

Now consider a second finite element geometry, identical to the previous cell except that additional matrix material, with a volume  $V_{matrix2}$ , has been evenly divided and added to the top and bottom of the first cell. Because of the size of the first cell, this additional matrix material is also unaffected by the presence of the wavy nanotube, thus the force necessary to produce a uniform strain  $\epsilon_z$  in this additional matrix material is simply  $F_2 = \frac{E_{mat} V_{mat2} \epsilon_z}{L}$ . The effective reinforcing modulus for the second finite element cell can be written as

$$E_{ERM_2} = \frac{\frac{(F_{tot} + F_2)L}{(V + V_{mat_2})} \square_z \frac{V_{mat} + V_{mat_2}}{V + V_{mat_2}} E_{mat}}{\frac{V_{NT}}{V + V_{mat_2}}} = \frac{(F_{tot} + F_2)L}{V_{NT} \square_z} \square_z \frac{V_{mat} + V_{mat_2}}{V_{NT}} E_{mat} \quad (15)$$

Substituting the expression for  $F_2$  into (15) yields  $E_{ERM1}=E_{ERM2}$ , and thus for a sufficiently large matrix the value of  $E_{ERM}$  is independent of the size of the finite element cell. For all simulations the finite element cell was created large enough such that this condition was satisfied; typically the nanotube volume fraction in the finite element cell was less than 0.05%.

### **Reduction of $E_{ERM}$ parameters for the finite element analysis**

Because we have shown that  $E_{ERM}$  converges given a sufficiently large finite element cell, it is sufficient to consider the model parameters that influence  $E_{cell}$  in the present analysis. Assuming isotropic behavior of the phase materials, the model at first appears to be dependent on seven parameters: the moduli ( $E_{NT}$  and  $E_{matrix}$ ) and Poisson ratios ( $\square_{NT}$  and  $\square_{matrix}$ ) of the phase materials, the wavelength and diameter of the NT ( $\square$  and  $d$ ), and the sinusoidal amplitude  $a$  such that

$$E_{cell} = f(E_{NT}, E_{matrix}, \square_{NT}, \square_{matrix}, a, d, \square). \quad (16)$$

To first simplify the analysis we assume that the Poisson ratios of the phases are identical and equal to 0.30, an assumption which we will discuss in further detail later in the text. Thus one can write (16) in a mathematically equivalent form as

$$g(E_{\text{cell}}, E_{\text{NT}}, E_{\text{matrix}}, a, d, \Pi) = 0, \quad (17)$$

where  $g$  is dependent on these six parameters but of an unknown functional form. Using the Buckingham Pi theorem (Fox and McDonald 1992), we can further rewrite (17) as

$$\Pi_1 = G_1(\Pi_2, \Pi_3, \Pi_4), \quad (18)$$

where  $\Pi_i$  are the dimensionless ratios

$$\begin{aligned} \Pi_1 &= E_{\text{NT}}^a \Pi^b E_{\text{cell}}, & \Pi_2 &= E_{\text{NT}}^c \Pi^d E_{\text{mat}} \\ \Pi_3 &= E_{\text{NT}}^e \Pi^f a, & \Pi_4 &= E_{\text{NT}}^g \Pi^h d \end{aligned} \quad (19)$$

The unknown superscript parameters  $a-h$  in (19) can be determined through dimensional analysis and substituted into (18) to yield

$$\frac{E_{\text{cell}}}{E_{\text{NT}}} = G_1 \left( \frac{E_{\text{NT}}}{E_{\text{mat}}}, \frac{a}{\Pi}, \frac{\Pi}{d} \right), \quad (20)$$

where  $G_1$  is a function of these parameters (only) and will be determined through our finite element study.

## **Micromechanical Modeling and the Mori-Tanaka Method**

We will illustrate how inclusion waviness can be incorporated into traditional micromechanical techniques by using the Mori-Tanaka method, a popular tool for the analysis of multi-phase materials (Mori and Tanaka 1973; Benveniste 1987; Weng 1990). The Mori-Tanaka method has been used by a wide range of researchers to model the effective behavior of composites, and allows the average stress fields and overall effective stiffness of a composite with a non-dilute concentration of inclusions to be determined. It has been used to study the effect of inclusion shape on composite moduli (Zhao and Weng 1990; Qui and Weng 1991) and the viscoelastic behavior of polymer-matrix composites (Brinson and Lin 1998; Fisher and Brinson 2001). Further, the Mori-Tanaka method has been extended to cover composites with multiple inclusion phases (Benveniste 1987; Weng 1990) and random orientations of inclusions (Tandon and Weng 1986; Weng 1990).

Specifically we are interested in the Mori-Tanaka solution for an  $N$  phase composite, where each inclusion phase is randomly orientated in two or three dimensional space. For the following derivation we first consider the case where the inclusions are unidirectionally aligned within the matrix. Once the necessary parameters have been determined for this case, appropriate tensor transformations and

volume averaging procedures will be introduced to account for the different inclusion orientations. This technique is described in more detail below.

### ***Mori-Tanaka method for unidirectionally-aligned inclusions***

We assume that the composite is comprised of  $N$  phases; the matrix will be denoted as phase  $0$  with a corresponding stiffness  $C_0$  and volume fraction  $f_0$ , while an arbitrary  $r$ th inclusion phase (where  $r=1$  to  $N-1$ ) has a stiffness of  $C_r$  and a volume fraction  $f_r$ . Each phase is assumed to be linearly elastic and isotropic, and perfect bonding between the inclusions and the matrix is assumed. The inclusions are further assumed to be ellipsoidal with a circular cross-section ( $a_1=a_2$ ), an aspect ratio  $\square_r$  (ratio of length to diameter), and aligned along the 3-axis (as shown in Figure 22).

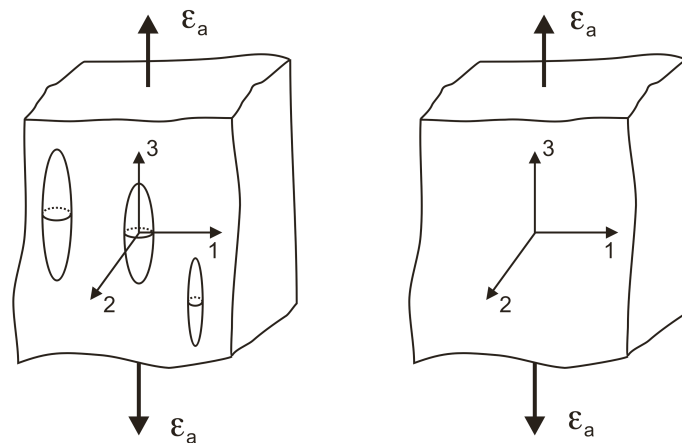


**Figure 22. Schematic of Mori-Tanaka method. (left) Multiphase composite material. (right) Comparison material.**

Consider the two models shown in Figure 22, representing the composite model and a “comparison material” with properties identical to those of the matrix. Unless required, explicit tensor notation will be omitted for clarity. Displacements are now prescribed on the boundary of each material to give rise to a uniform strain  $\epsilon_a$  in each material. The stresses required to produced this uniform strain in each material are

$$\bar{\sigma} = C\epsilon_a, \quad \bar{\sigma}_0 = C_0\epsilon_a \quad (21)$$

where  $\bar{\sigma}$  and  $\bar{\sigma}_0$  are the average stress of the composite and comparison materials, respectively.

The strain field within the matrix material of the composite will not be uniform due the presence of the inclusions (and hence the average matrix strain  $\bar{\epsilon}_b$  will not equal  $\epsilon_a$ ), but rather will be perturbed by an amount  $\bar{\epsilon}_b^{pt}$  such that

$$\bar{\epsilon}_b = \epsilon_a + \bar{\epsilon}_b^{pt}, \quad (22)$$

where an overscore represents the volume average of the stated quantity. The average strain in the  $r$ th inclusion is further perturbed from that of the matrix,

$$\bar{\epsilon}_r = \bar{\epsilon}_b + \bar{\epsilon}_r^{pt}. \quad (23)$$

Given that the average stress in each phase is given as  $\bar{\sigma}_r = C_r \bar{\epsilon}_r$ , using the equivalent inclusion method one can show that the average stress in the  $r$ th inclusion can be written in terms of the matrix stiffness,

$$\bar{\sigma}_r = C_r \bar{\epsilon}_r = C_0 \left( \bar{\epsilon}_r + \bar{\epsilon}_r^* \right), \quad (24)$$

where  $\bar{\epsilon}_r^*$  is the fictitious eigenstrain of the  $r$ th inclusion. For a single ellipsoidal inclusion in an infinite matrix, Eshelby showed that the eigenstrain and perturbed strain of the  $r$ th inclusion can be related via

$$\bar{\epsilon}_r^{\text{pt}} = S_r \bar{\epsilon}_r^*, \quad (25)$$

where  $S_r$  is the Eshelby tensor. General forms of the Eshelby tensor are provided in the Appendix.

Solving for  $\bar{\epsilon}_r^*$  in (24) and then substituting into (23) using (25), one can find the dilute strain-concentration factor of the  $r$ th phase,  $A_r^{\text{dil}}$ , which relates the average strain in the  $r$ th inclusion to the average strain in the matrix, such that

$$\bar{\epsilon}_r = A_r^{\text{dil}} \bar{\epsilon}_0, \quad (26)$$

where

$$A_r^{\text{dil}} = \left[ \mathbf{I} + S_r C_0^{-1} (C_r - C_0) \right]^{-1} \quad (27)$$

and  $\mathbf{I}$  is the fourth order identity tensor. We further require that the volume-weighted average phase strains must equal the far-field applied strain, such that

$$f_0 \bar{\boldsymbol{\epsilon}} + \sum_{r=1}^{N_{\text{I}}} f_r \boldsymbol{\epsilon}_r = \bar{\boldsymbol{\epsilon}}. \quad (28)$$

Given (28), we can now define the strain-concentration factor  $A_0$ , which accounts for inclusion interaction by relating the average matrix strain in the composite to the uniform applied strain,

$$\bar{\boldsymbol{\epsilon}} = A_0 \boldsymbol{\epsilon}_a, \quad (29)$$

where

$$A_0 = f_0 \mathbf{I} + \sum_{r=1}^{N_{\text{I}}} f_r A_r^{\text{dil}}. \quad (30)$$

The key assumption of the Mori-Tanaka method is that the far-field strain that each inclusion “feels” is the unknown average matrix strain. This can be expressed as

$$\boldsymbol{\epsilon}_r = A_r^{\text{dil}} \bar{\boldsymbol{\epsilon}}, \quad (31)$$

which in conjunction with (29) gives the strain-concentration factor  $A_r$  for the  $r$ th inclusion phase in the *non-dilute composite* as

$$A_r = A_r^{\text{dil}} A_0. \quad (32)$$

To find the effective stiffness  $C$  for a unidirectionally aligned composite, we require that the average stress  $\bar{\sigma}$  of the composite be equal to the sum of the weighted average stresses in each phase,

$$\bar{\sigma} = f_0 \sigma_0 + \sum_{r=1}^{N-1} f_r \sigma_r = C \bar{\epsilon}. \quad (33)$$

Through straightforward substitution and manipulation, the effective stiffness of the unidirectionally aligned composite is found to be

$$C = f_0 C_0 A_0 + \sum_{r=1}^{N-1} f_r C_r A_r. \quad (34)$$

For purposes of the next section it will be useful to express (34) in a slightly different form. Recalling (28) and (33), we can write

$$C = \begin{bmatrix} \sigma \\ \sigma \\ \sigma \end{bmatrix} = f_0 C_0 + \sum_{r=1}^{N-1} f_r C_r A_r^{\text{dil}} \begin{bmatrix} \sigma \\ \sigma \\ \sigma \end{bmatrix} = f_0 I + \sum_{r=1}^{N-1} f_r A_r^{\text{dil}} \begin{bmatrix} \sigma \\ \sigma \\ \sigma \end{bmatrix}, \quad (35)$$

which is a form prevalent in the literature (see (Weng 1990)).<sup>4</sup> Both (34) and (35) thus provide the effective stiffness of a multiphase composite with aligned inclusions. However, in order to account for random orientations of the inclusion phases, the analysis must be extended as discussed below.

### ***Mori-Tanaka method for randomly aligned inclusions***

When the inclusion phases are randomly orientated in the matrix, determination of the effective composite stiffness can be accomplished by taking the orientational averages of appropriate quantities (Weng 1990). In this case the strain consistency condition in (28) can be written as

$$\begin{bmatrix} \sigma \\ \tau \end{bmatrix} = f_0 \mathbf{I} + \sum_{r=1}^{N-1} f_r \{ A_r^{dil} \} \begin{bmatrix} \sigma \\ \tau \end{bmatrix} = \langle \sigma_a \rangle \quad (36)$$

where brackets  $\{ \}$  represent the average of a quantity over all possible orientations.<sup>5</sup> Due to this averaging process, the average strain in the matrix will be different from that in the unidirectional composite due to the random alignment of inclusions.

---

<sup>4</sup> Weng further simplifies this expression using the relationship that  $A_0^{dil} = \mathbf{I}$ . Such an expression is sensible given that by definition  $A_0$  relates the average strain in the matrix to the uniform applied strain. In the dilute sense these strains will be equal.

<sup>5</sup> Note that the derivation for unidirectional inclusions presented in the last section is a subset of the more general derivation presented here.

Similarly one can rewrite (33) for the case of randomly orientated inclusions (with the understanding that the matrix stress and strain are orientation-independent due to the isotropy of the matrix) as

$$\bar{\epsilon} = f_0 \epsilon_0 + \sum_{r=1}^{N-1} f_r \{ \epsilon_r \} = C \epsilon_h. \quad (37)$$

This expression can be simplified using the relationships established in the preceding section. Briefly,

$$\begin{aligned} \bar{\epsilon} &= f_0 C_0 \epsilon_b + \sum_{r=1}^{N-1} f_r \{ C_r \epsilon_r \} \\ &= f_0 C_0 \epsilon_b + \sum_{r=1}^{N-1} f_r \{ C_r A_r^{dil} \} \epsilon_b \\ &= \begin{bmatrix} \epsilon_b \\ \epsilon_b \\ \epsilon_b \end{bmatrix} f_0 C_0 + \sum_{r=1}^{N-1} f_r \{ C_r A_r^{dil} \} \begin{bmatrix} \epsilon_b \\ \epsilon_b \\ \epsilon_b \end{bmatrix} = C \epsilon_h \end{aligned} \quad (38)$$

From (36) and (38), the effective stiffness of a composite with randomly orientated inclusions can be written as

$$C = \begin{bmatrix} \epsilon_b \\ \epsilon_b \\ \epsilon_b \end{bmatrix} f_0 C_0 + \sum_{r=1}^{N-1} f_r \{ C_r A_r^{dil} \} \begin{bmatrix} \epsilon_b \\ \epsilon_b \\ \epsilon_b \end{bmatrix} f_0 I + \sum_{r=1}^{N-1} f_r \{ A_r^{dil} \} \begin{bmatrix} \epsilon_b \\ \epsilon_b \\ \epsilon_b \end{bmatrix}, \quad (39)$$

which is the direct analog of (35) except that appropriate averaging is used here to account for the inclusion orientation. Later in this chapter we will discuss how these orientational averages can be determined.

### **Euler angles and tensor transformations**

To determine the effective properties of a composite with randomly orientated inclusions, it will be necessary to calculate various orientational averages as outlined in the previous section. We will assume that the local axes of the fiber are denoted  $x'_1$ ,  $x'_2$ , and  $x'_3$  (where  $x'_3$  is the inclusion axis), and the global (or fixed) composite coordinates are  $X_1$ ,  $X_2$ , and  $X_3$  (see Figure 23). Our goal is to develop the transformation matrix  $a_{ij}$  which maps vector  $v'_j$  in the local coordinate system to coordinates  $v_i$  in the global coordinate system via

$$v_i = a_{ij} v'_j. \quad (40)$$

Note that in general it is necessary to specify three Euler angles to describe the inclusion orientation; however, because the inclusion is assumed to be spheroidal it is only necessary to specify  $\theta$  and  $\phi$  in Figure 23 to completely describe the orientation of the fiber.

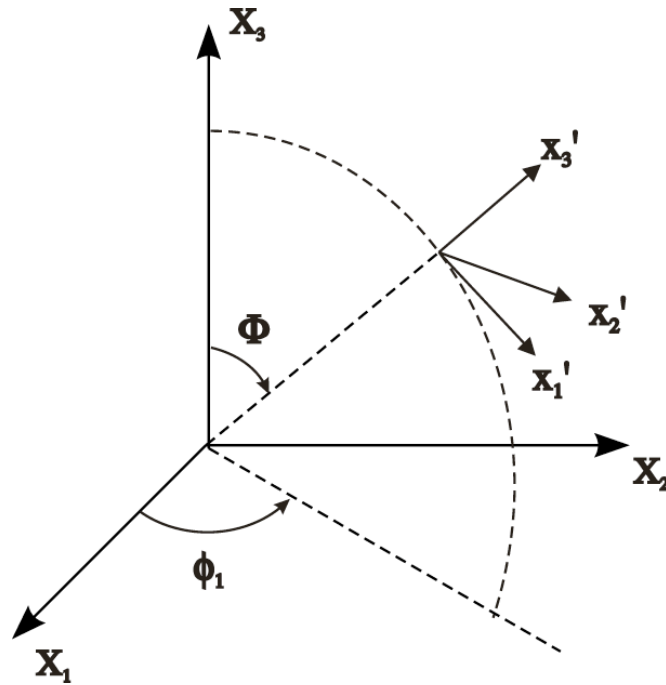


**Figure 23. Relationship between the local and global coordinate systems.**

Following Roe's specification for Euler angles (Randle 1992), the local coordinate system is obtained by a rotation of  $\phi_1$  about the  $X_3$  axis, followed by a rotation of  $\phi$  about the resulting  $x_2'$  axis. These rotations can be described using the appropriate coordinate transformations that map *local* vectors to *global* vectors (i.e. where  $X_i = R_{ij} x_j'$ )

$$R(\phi_1) = \begin{bmatrix} \cos(\phi_1) & \sin(\phi_1) & 0 \\ \sin(\phi_1) & \cos(\phi_1) & 0 \\ 0 & 0 & 1 \end{bmatrix}, \quad R(\phi) = \begin{bmatrix} \cos(\phi) & 0 & \sin(\phi) \\ 0 & 1 & 0 \\ \sin(\phi) & 0 & \cos(\phi) \end{bmatrix}. \quad (41)$$

Consecutive rotations of  $\alpha_1$  and  $\alpha$  thus result in the following transformation between local and global coordinates:

$$\begin{bmatrix} X_1 \\ X_2 \\ X_3 \end{bmatrix} = R(\alpha_1)R(\alpha) \begin{bmatrix} x_1 \\ x_2 \\ x_3 \end{bmatrix} = \begin{bmatrix} mp & n & mq \\ np & m & nq \\ q & 0 & p \end{bmatrix} \begin{bmatrix} x_1 \\ x_2 \\ x_3 \end{bmatrix} = a_{ij}^{3D} x_j \quad (42)$$

where  $m = \cos(\alpha_1)$ ,  $n = \sin(\alpha_1)$ ,  $p = \cos(\alpha)$ ,  $q = \sin(\alpha)$ , and  $a_{ij}^{3D}$  represents the transformation matrix describing transformations in full three-dimensional space. If the inclusions are restricted to lie in the 1-2 plane, the appropriate 2D transformation matrix  $a_{ij}^{2D}$  can be found by setting  $\alpha = \pi/2$  (see Figure 23), such that

$$a_{ij}^{2D} = \begin{bmatrix} 0 & \sin \alpha_1 & \cos \alpha_1 \\ 0 & \cos \alpha_1 & \sin \alpha_1 \\ 1 & 0 & 0 \end{bmatrix}. \quad (43)$$

Higher order tensor transformations are accomplished through the usual tensor transformation laws. Thus the transformation of a fourth-order stiffness tensor  $B_{ijkl}$  from local to global coordinates can be written as

$$B_{ijkl}(\alpha_1, \alpha) = a_{ir} a_{js} a_{kt} a_{lu} B'_{rstu}, \quad (44)$$

where the angular dependence of the  $a_{ij}$  terms is implied and the standard convention that double indices implies summation is used.<sup>6</sup> To further illustrate (44), we write out the  $B_{1111}$  terms below:

$$B_{1111}(\square_1, \square) = a_{11}^4 B'_{1111} + a_{12}^4 B'_{2222} + a_{13}^4 B'_{3333} + (2B'_{1122} + 4B'_{1212}) a_{11}^2 a_{12}^2 + (2B'_{1133} + 4B'_{1313}) a_{11}^2 a_{13}^2 + (2B'_{2233} + 4B'_{2323}) a_{12}^2 a_{13}^2, \quad (45)$$

where it is assumed that particular symmetry conditions ( $B_{rstu}=B_{turs}$  and  $B_{rstu}=B_{rsut}=B_{srut}=B_{srtu}$ ) hold in the local coordinate system. When these symmetry conditions do not hold (such as for the dilute strain concentration tensor  $A_r^{\text{dil}}$  in the previous section) the procedure is identical, although the collection of terms such as that in (45) is more tedious.

Given (44), the orientational average of a fourth tensor in random 3D space is

$$\{B_{ijkl}\} = \frac{1}{2\pi} \int_0^\pi \int_0^{2\pi} B_{ijkl}(\square_1, \square) \sin(\square) d\square d\square_1 \quad (46)$$

where the transformation matrix for three dimensional space  $a_{ij}^{3D}$  is used in (44) and the  $\sin(\square)$  term accounts for the surface area of a sphere. For a 3D random orientation

---

<sup>6</sup> We stress that the transformation in (44) is a *tensor* transformation, and as such is only applicable to tensor quantities. Quantities which are not of tensorial form, specifically tensors expressed using contracted notation, must first be converted to their appropriate tensorial components before such a transformation is valid.



$$\begin{aligned}
\{B_{11}\} = \{B_{22}\} &= \frac{1}{8} [3B_{22} + 3B_{33} + B_{23} + B_{32} + 4B_{44}] \\
\{B_{33}\} &= B_{11} \\
\{B_{12}\} = \{B_{21}\} &= \frac{1}{8} [B_{22} + B_{33} + 3B_{23} + 3B_{32} - 4B_{44}] \\
\{B_{13}\} = \{B_{23}\} &= \frac{1}{2} [B_{21} + B_{31}] \\
\{B_{31}\} = \{B_{32}\} &= \frac{1}{2} [B_{12} + B_{13}] \\
\{B_{44}\} = \{B_{55}\} &= \frac{1}{2} [B_{55} + B_{66}] \\
\{B_{66}\} &= \frac{1}{8} [B_{22} + B_{33} - B_{23} - B_{32} + 4B_{44}]
\end{aligned} \tag{49}$$

### A note on symmetry

Writing the constitutive stress-strain relationship  $\sigma_{ij} = C_{ijkl} \epsilon_{kl}$  in tensor form suggests that it would require 81 constants to characterize the stress-strain response of a material (i.e there are 81 independent  $C_{ijkl}$  tensor components). However, the condition that the stress and strain tensors are symmetric reduces the number of independent constants to 36; this allows the use of contracted notation that is commonplace in composites research (see the Appendix). The number of independent constants is further reduced based on arguments related to the work per unit volume of the system, from which one can prove that the stiffness (compliance) tensor must be symmetric, such that  $C_{ijkl} = C_{klij}$ . This condition further reduces the number of independent constants to 21. The number of independent constants can be further

reduced based on assumptions of the material behavior (i.e. it can be shown that transversely isotropic materials have 5 independent constants, and that isotropic materials have two independent constants).

One inconsistency with the implementation of the Mori-Tanaka method for multiphase materials is that it may yield non-symmetric stiffness (and compliance) tensors, thus violating the symmetry conditions required for a *real* material (Benveniste, Dvorak et al. 1991; Li 1999; Schjodt-Thomsen and Pyrz 2001). This non-symmetry is a result of the non-symmetric strain concentration tensors  $A_r^{\text{dil}}$  calculated in (27). This difficulty has been attributed to the extension of the Mori-Tanaka scheme, originally developed for two-phase materials, to multiphase composites (Li 1999).

To illustrate, we calculate the effective stiffness of a three-phase composite composed of isotropic phase materials. Here we consider cylindrical inclusions with an aspect ratio  $\square=L/d=1000$ , randomly orientated in the 1-2 plane with volume fractions  $f_0=0.50$  and  $f_1=f_2=0.25$ , phase moduli  $E_0=1$ ,  $E_1=50$ , and  $E_2=200$ , and Poisson ratios  $\square_i=0.30$ , where the matrix phase is denoted as phase  $0$ . Using the Mori-Tanaka method, the effective stiffness of the system can be calculated as

$$L_{2D} = \begin{bmatrix} 36.764 & 12.214 & 1.350 & 0 & 0 & 0 \\ 12.214 & 36.764 & 1.350 & 0 & 0 & 0 \\ 1.342 & 1.342 & 3.222 & 0 & 0 & 0 \\ 0 & 0 & 0 & 1.039 & 0 & 0 \\ 0 & 0 & 0 & 0 & 1.039 & 0 \\ 0 & 0 & 0 & 0 & 0 & 12.275 \end{bmatrix} \quad (50)$$

where the non-symmetry of stiffness tensor ( $L_{13}=L_{23} \neq L_{31}=L_{32}$ ) is evident (see also Schjodt-Thomsen and Pyrz (2001) for additional examples). Such an example is only given to illustrate the non-symmetry of the stiffness tensor; the extent of non-symmetry is closely related to the properties and geometries of the phases in a particular system. It is worth noting the following conditions, under which the Mori-Tanaka method is guaranteed to yield a symmetric stiffness (Schjodt-Thomsen and Pyrz 2001):

- Two-phase composites
- Multiphase composites with aligned inclusions
- Multiphase composites with randomly aligned spherical inclusions

In addition, in our numerical studies we have found that the Mori-Tanaka solution for a multiphase composite with similarly shaped inclusions randomly orientated in three-dimensional space has in every case yielded a symmetric (and isotropic) stiffness; however, a proof of this condition is beyond the scope of this dissertation.

One of the manners in which the symmetry of the effective stiffness can be guaranteed is by normalizing the concentration tensors (see Schjodt-Thomsen and Pyrz (2001) and references therein). However, because here we are primarily interested in the effective moduli predictions (rather than the stiffness tensor), one can show that the effect of this non-symmetry is minimal. Specifically, later in this chapter we show that the effective moduli are only dependent on the product of the  $C_{13}$  and  $C_{31}$  terms, independent of the symmetry (or lack thereof) of the stiffness tensor. Thus symmetry of the stiffness tensor was enforced *after* the Mori-Tanaka calculation by setting

$$C_{13} = C_{23} = C_{31} = C_{32} = \sqrt{C_{13} C_{31}}. \quad (51)$$

Such manipulation will have no affect on the Mori-Tanaka predictions for  $E_{11}$ ,  $E_{33}$ ,  $\nu_{12}$ , or  $\nu_{13}$ .

### **An alternate model for randomly orientated inclusions**

An alternative method has been proposed in the literature to determine the effective moduli of composites containing randomly orientated inclusions using the Mori-Tanaka method (Huang 2001). This alternative model will be referred to as the Huang model, to distinguish it from the Weng model described earlier. In the Huang model, the effective stiffness for a multiphase composite is found by taking the

orientational average of the effective modulus for the unidirectional composite case (i.e. equation (35)), rather than the orientational averaging of the individual components as outlined in (39) for the Weng model.

The Huang model is inviting because it allows explicit expressions for composites with randomly oriented inclusions to be given in terms of the unidirectional composite stiffness components. However, there is a critical difference between these models. For the Weng model, the introduction of the orientational averaging of field quantities is effectively introduced *before* the determination of the unknown average matrix strain that is fundamental to the Mori-Tanaka approach. For the Huang model, the unknown matrix strain is solely determined from the analysis of the unidirectional composite model, and thus is not dependent on the type of randomness that the inclusions might exhibit. Thus the Huang model does not properly model a multiphase composite with randomly orientated inclusions, but rather models a composite within which individual domains of aligned inclusions are present. As shown in Figure 24, for the Huang model the inclusion orientations are random in the sense that these smaller domains of aligned inclusions are of different orientations within the global material.

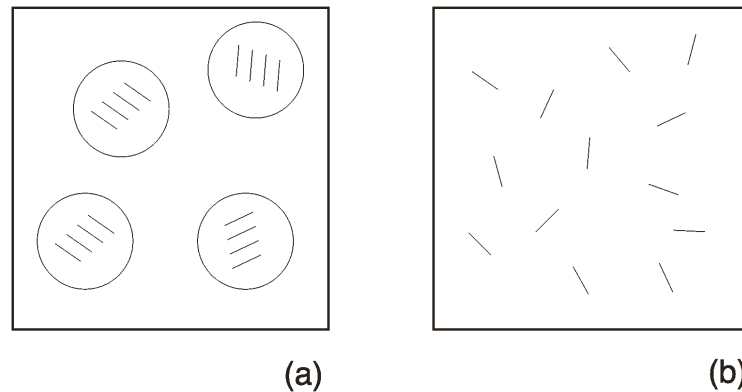


**Figure 24. Models to account for randomness of inclusion orientation. (a) Huang model. (b) Weng model.**

For small volume fractions of inclusions, and when the properties of the inclusions are not vastly different than those of the matrix, results from the two models are somewhat similar. However, this difference becomes significant as the volume fractions of inclusions increase, due to the difference between the two models in the determination of the average matrix strain of the composite. (We note that in the case of 2D random orientations the out-of-plane predictions from each model are in excellent agreement.) To illustrate the difference in moduli predictions between the two methods, the results for a three-phase composite consisting of isotropic phase constituents, with equal volume fractions of inclusion phases (i.e.  $f_1=f_2$ ), are presented in Table 6. Here we see that the effective moduli found using the Huang model are *less* than those found from the (correct) Weng Mori-Tanaka implementation, because the Huang model overestimates the average matrix strain, leading to a model of

material behavior that is too compliant. Because the Weng model correctly accounts for inclusion orientation in its determination of the effective composite stiffness, all subsequent work utilizing the Mori-Tanaka method will use the Weng model, i.e. equation (39), for the determination of the effective composite properties.

		Weng model		Huang model	
		$f_0=0.9$	$f_0=0.6$	$f_0=0.9$	$f_0=0.6$
3D random orientation	E	10.99	55.74	10.19	38.13
	$\nu$	4.37	22.19	4.06	15.23
	$\nu$	0.256	0.256	0.256	0.252
2D random orientation	$E_{11}=E_{22}$	20.44	99.80	19.18	74.15
	$E_{33}$	1.53	2.61	1.53	2.60
	$\nu_{12}$	7.68	37.62	7.21	27.85
	$\nu_{13}=\nu_{23}$	0.46	0.83	0.46	0.83
	k	15.53	74.56	14.61	55.91

**Table 6. Comparison of Huang and Weng models for effective moduli of multiphase composites with randomly orientated inclusions. ( $f_1=f_2$ ,  $E_0=1$ ,  $E_1=100$ ,  $E_2=1000$ ,  $\nu_1=\nu_2=L/d=1000$ , and  $\nu_3=0.30$ )**

### Simplification for a two-phase system

While the above formulations are concerned with the effective properties of multiphase composite materials, analytical expressions have been derived for the Mori-Tanaka solution for two-phase composites with 2D and 3D randomly orientated

inclusions (Tandon and Weng 1986). The expressions are quite unwieldy and thus not repeated here. It has been verified numerically that the Weng multiphase composite model used in this work matches the results of the analytical expressions for two-phase composites.

***Determination of the effective engineering constants***

Keeping in mind the preceding arguments that require a contracted stiffness tensor for a *real* material to be symmetric, the stress-strain relationship for a transversely isotropic material with a 1-2 plane of isotropy can be written as

$$\begin{matrix} \square_1 \\ \square_2 \\ \square_3 \\ \square_4 \\ \square_5 \\ \square_6 \end{matrix} = \begin{bmatrix} C_{11} & C_{12} & C_{13} & 0 & 0 & 0 \\ C_{12} & C_{11} & C_{13} & 0 & 0 & 0 \\ C_{31} & C_{31} & C_{33} & 0 & 0 & 0 \\ 0 & 0 & 0 & C_{44} & 0 & 0 \\ 0 & 0 & 0 & 0 & C_{44} & 0 \\ 0 & 0 & 0 & 0 & 0 & \frac{C_{11} - C_{12}}{2} \end{bmatrix} \begin{matrix} \square_1 \\ \square_2 \\ \square_3 \\ \square_4 \\ \square_5 \\ \square_6 \end{matrix} \tag{52}$$

where the tensorial shear strains  $\square$  are related to the engineering shear strains  $\square$  via  $\square_4 = \square_{23} = 2\square_{23}$ ,  $\square_5 = \square_{13} = 2\square_{13}$ , and  $\square_6 = \square_{12} = 2\square_{12}$ . For completeness, a more detailed description of contracted notation is provided in the Appendix. The contracted stiffness for a composite with inclusions aligned along the 3-axis, as well as composites with inclusions randomly orientated in the 1-2 plane, will show such a

form. For the case of inclusions randomly orientated in three-dimensional space, the stiffness will be fully isotropic such that the additional relations  $C_{11}=C_{33}$ ,  $C_{12}=C_{13}=C_{31}=C_{32}$ , and  $C_{44}=\frac{1}{2}(C_{11} - C_{12})$  in (52) will be satisfied.

The compliance tensor  $S$  (where  $\square=S\square$ ) is defined as the inverse of the stiffness tensor, and can be written in terms of the stiffness components  $C_{ij}$  as

$$S = \begin{pmatrix} \frac{C_{11}C_{33} - C_{13}C_{31}}{\square_1} & \frac{C_{12}C_{33} - C_{13}C_{31}}{\square_1} & \frac{C_{13}}{\square_2} & 0 & 0 & 0 \\ \frac{C_{12}C_{33} - C_{13}C_{31}}{\square_1} & \frac{C_{11}C_{33} - C_{13}C_{31}}{\square_1} & \frac{C_{13}}{\square_2} & 0 & 0 & 0 \\ \frac{C_{13}}{\square_2} & \frac{C_{13}}{\square_2} & \frac{C_{11} + C_{12}}{\square_2} & 0 & 0 & 0 \\ 0 & 0 & 0 & \frac{1}{C_{44}} & 0 & 0 \\ 0 & 0 & 0 & 0 & \frac{1}{C_{44}} & 0 \\ 0 & 0 & 0 & 0 & 0 & \frac{2}{C_{11} - C_{12}} \end{pmatrix} \quad (53)$$

where

$$\begin{aligned} \square_1 &= C_{33}(C_{11}^2 - C_{12}^2) - 2C_{13}C_{31}(C_{11} - C_{12}) \\ \square_2 &= C_{33}(C_{11} + C_{12}) - 2C_{13}C_{31} \end{aligned} \quad (54)$$

From (52)-(54), we see that the procedure of using the geometric mean of  $C_{13}$  and  $C_{31}$  given in (51) to enforce the symmetry of the Mori-Tanaka effective stiffness will only affect the  $S_{13}=S_{23}=S_{31}=S_{31}$  compliance components. While such changes will alter the

exact value of some of the engineering constants, for our purposes the Young's and shear moduli with which we are most interested will not be affected by such a scheme. We note that the compliance tensor will have the same level of symmetry as that of the stiffness tensor.

Once the stiffness and compliance tensors are known, the components of these tensors can be used to calculate the engineering constants of the material. For an isotropic material two independent constants are required to describe the material response, for example the Young's modulus  $E$  and the shear modulus  $\mu$ . These can be determined from the known stiffness (or compliance) terms via

$$\begin{aligned} E = E_{11} = E_{22} = E_{33} &= \frac{1}{S_{11}} = \frac{\nu_1}{C_{11}C_{33} - C_{13}C_{31}} \\ \mu = \mu_{44} = \mu_{55} = \mu_{66} &= \frac{1}{S_{44}} = C_{44} \end{aligned} \quad (55)$$

For a transversely isotropic material five independent constants are required to fully characterize the material response. For a transversely isotropic material with a 1-2 plane of isotropy, five such constants are the transverse modulus  $E_{11}=E_{22}$ , the longitudinal modulus  $E_{33}$ , the axial shear modulus  $\mu_{44}=\mu_{55}$ , the transverse shear modulus  $\mu_{66}$ , and the plane strain bulk modulus  $k$ , which can be determined from the known stiffness or compliance terms such that

$$\begin{aligned}
E_{11} = E_{22} &= \frac{1}{S_{11}} = \frac{\nu_1}{C_{11}C_{33} - C_{13}C_{31}} \\
E_{33} &= \frac{1}{S_{33}} = \frac{\nu_2}{C_{11} + C_{12}} \\
\nu_{44} = \nu_{55} &= \frac{1}{S_{44}} = C_{44} \\
\nu_{66} &= \frac{1}{S_{66}} = \frac{2}{C_{11} - C_{12}} \\
k &= \frac{C_{11} + C_{12}}{2}
\end{aligned} \tag{56}$$

Relationships to obtain alternative elastic constants are given in the Appendix.

## Discretization of nanotubes based on waviness

To model the nanotube-reinforced polymer we partition the nanotube inclusions into distinct phases, based on their embedded waviness, and treat the problem as that of a multiphase composite. Each nanotube phase is then assigned a distinct effective reinforcing modulus  $E_{ERM}$  based on the average waviness of the phase and the results of the preceding finite element analysis. In practice, such a solution could be developed by imaging a representative portion of the NRP and developing an appropriate waviness distribution function characterizing the magnitude and extent of the nanotube waviness, leading to an appropriate multiphase composite model (see Figure 25 and Figure 26). This waviness distribution, along with the spatial

orientation of the NTs, can be used within an appropriate micromechanical method to provide a refined estimate of the effective moduli of a nanotube-reinforced polymer. This procedure is demonstrated in the next section using the Mori-Tanaka method for 2D and 3D randomly orientated inclusions assuming a given distribution of nanotube waviness.

Before we begin our analysis, it is insightful to estimate the range of values that may be characteristic of the waviness and wavelength ratios associated with the wavy geometry of embedded nanotubes. For illustrative purposes, Figure 25 shows an image of an NRP with different wavy nanotubes marked by solid lines, with approximate values for  $a/\lambda$  and  $\lambda/d$  given in the inset. Several nanotubes in Figure 25 are approximately straight (and not identified in the inset), while others show kinks and bends which, while not of the sinusoidal shape assumed in the model, will similarly limit the effective reinforcement of those nanotubes. We note that waviness perpendicular to the plane of the TEM image is masked, and that NT straightening during the preparation of the TEM sample may have occurred. Thus the waviness parameters shown in Figure 25 are to be seen as *illustrative* only, and will be influenced by the NRP system and the processing conditions of a particular sample. While a more thorough procedure to determine the embedded nanotube waviness may be warranted, for the purposes of this paper a hypothetical waviness distribution is sufficient to show the effect of nanotube waviness on the effective modulus of an

NRP. As our earlier analysis indicated, even for moderate nanotube waviness the decrease in effective reinforcement can be appreciable.

A critical step in the analysis is the determination of the dilute strain-concentration tensor  $A_r^{\text{dil}}$  relating the average strain of the  $r$ th inclusion to that of the matrix. In the present analysis  $A_r^{\text{dil}}$  is found via (27), where the stiffness tensor(s) of the inclusion phase(s)  $C_r$  are assumed to be isotropic with moduli  $E_{\text{ERM}}$  (based on the finite element modeling described earlier) and the Poisson ratio of the straight inclusion. The Eshelby tensors  $S_r$  are calculated assuming infinitely long cylindrical inclusions. Thus to account for the waviness of a particular inclusion we first find  $E_{\text{ERM}}$ , based on the embedded geometry and other applicable parameters, via a finite element analysis. We then treat the wavy inclusion as a straight inclusion but with an adjusted stiffness tensor to account for the wavy geometry. In related work discussed in the next section, we show that  $A_r^{\text{dil}}$  can be computed *directly* from an appropriate finite element analysis (Bradshaw, Fisher et al. 2002); in either case once  $A_r^{\text{dil}}$  has been determined the implementation of the Mori-Tanaka solution remains unchanged.

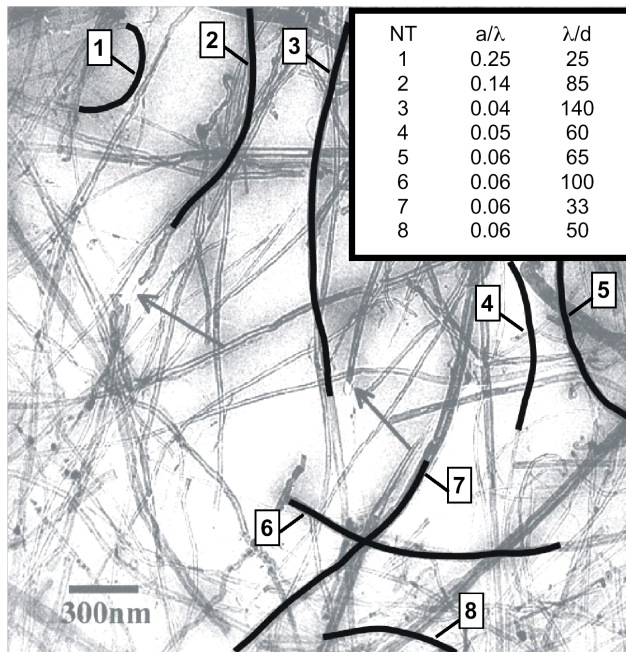


**Figure 25. Illustrative example of nanotube waviness. (Image from (Qian, Dickey et al. 2000)). (inset) Approximate values for the parameters  $w=a/\lambda$  and  $\lambda/d$  for the highlighted nanotubes.**

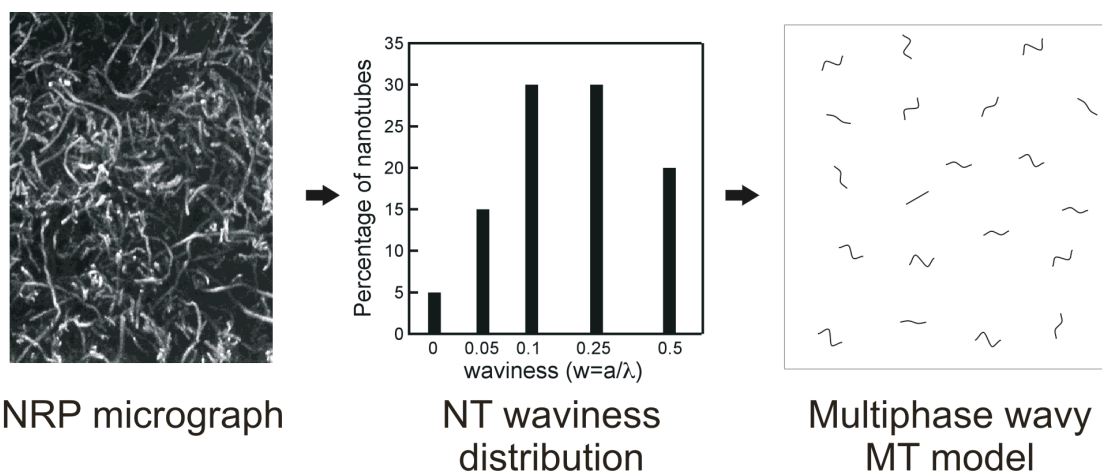


**Figure 26. Model of an NRP using a multiphase composite analysis with a known waviness distribution function.**

Our results suggest that modeling the NTs as straight inclusions (i.e. neglecting the curvature of the embedded geometry) is a simplification that will severely overestimate the reinforcement that the NTs provide the polymer. While the procedure here is demonstrated using  $E_{ERM}$  calculations based on finite element results, alternative means to evaluate  $E_{ERM}$ , such as molecular dynamics or related methods (Odegard, Gates et al. 2001a), could also be used in a similar analysis. Adaptations of the current model to include such effects as inter-layer (MWNTs) and inter-tube (NT bundles) sliding, as well as imperfect bonding between the nanotubes and the polymer, while not addressed here could also be developed.

## Results

The objective of this work is to develop a method to incorporate the typically observed waviness of embedded nanotubes into standard micromechanics techniques. Because the nanotube has been modeled as a continuum, the method is also in general applicable to other types of inclusions that may exhibit similar embedded geometries. We note that  $E_{ERM}$  will be less than (or equal to) the true NT modulus due to its waviness, and that a distribution of NT waviness within the material is likely. Thus rather than treat the NRP as a two-phase (nanotube/polymer) composite, we have developed a multiphase composite model where the NTs are partitioned into distinct

phases, with each NT phase assigned a characteristic  $E_{ERM}$  based on their embedded waviness.

With this in mind, the remainder of this section is divided into two parts. In the first part we discuss the impact of nanotube waviness and other model parameters on  $E_{ERM}$ . We will then use the results of the  $E_{ERM}$  analysis to compare the predictions of our micromechanical analysis, accounting for the embedded nanotube geometry, with results obtained assuming straight nanotube inclusions and with published experimental data for NRP effective modulus.

### ***Effective reinforcing modulus $E_{ERM}$***

As discussed previously, we have shown that the model for  $E_{ERM}$  is a function of three parameters: the waviness ( $w=a/\lambda$ ) and wavelength ratio ( $\lambda/d$ ) of the nanotube and the ratio of the phase moduli ( $E_{ratio}=E_{NT}/E_{matrix}$ ). Figure 27 shows  $E_{ERM}$  as a function of waviness for several different values of  $E_{ratio}$  and a wavelength ratio of 100. For all simulations a matrix modulus of 1 GPa was used. As expected, for zero waviness we obtain the straight nanotube results  $E_{ERM}=E_{NT}$ . We note that  $E_{ERM}$  is strongly dependent on the waviness and quickly decreases with increasing nanotube curvature. This drop in  $E_{ERM}$  is less pronounced for smaller  $E_{ratio}$  values because the mechanical constraint of the surrounding matrix material in this case is more significant.

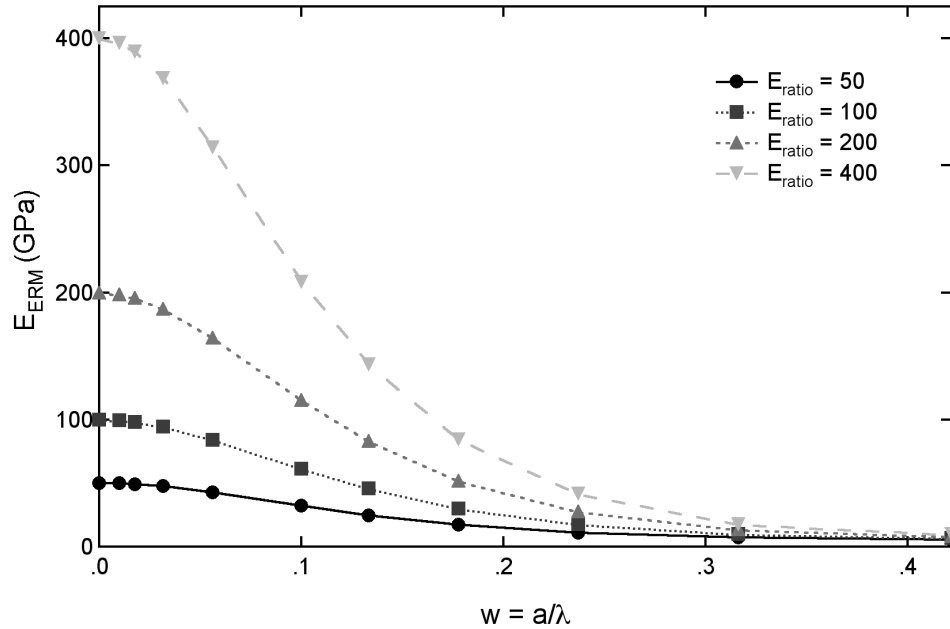


**Figure 27.  $E_{ERM}$  as a function of nanotube waviness ratio ( $a/\lambda$ ) for different ratios of phase moduli with wavelength ratio  $\lambda/d=100$ .  $E_{matrix}=1$  GPa.**

Figure 28 shows the dependence of  $E_{ERM}$  on the nanotube wavelength ratio for different values of waviness and  $E_{ratio}=200$ . We see that as the wavelength ratio increases the value of  $E_{ERM}$  converges to a constant value that is a function of the waviness. While we have shown that for longer wavelength ratios ( $\lambda/d > 1000$ ) curves of  $E_{ERM}$  versus waviness for different values of  $E_{ratio}$  can be superposed via vertical shifting (as discussed later in this section), for real NRP materials the wavelength ratio is likely to be much smaller. Unless otherwise specified, to simplify the remainder of this section we will only consider wavelength ratios of 100.

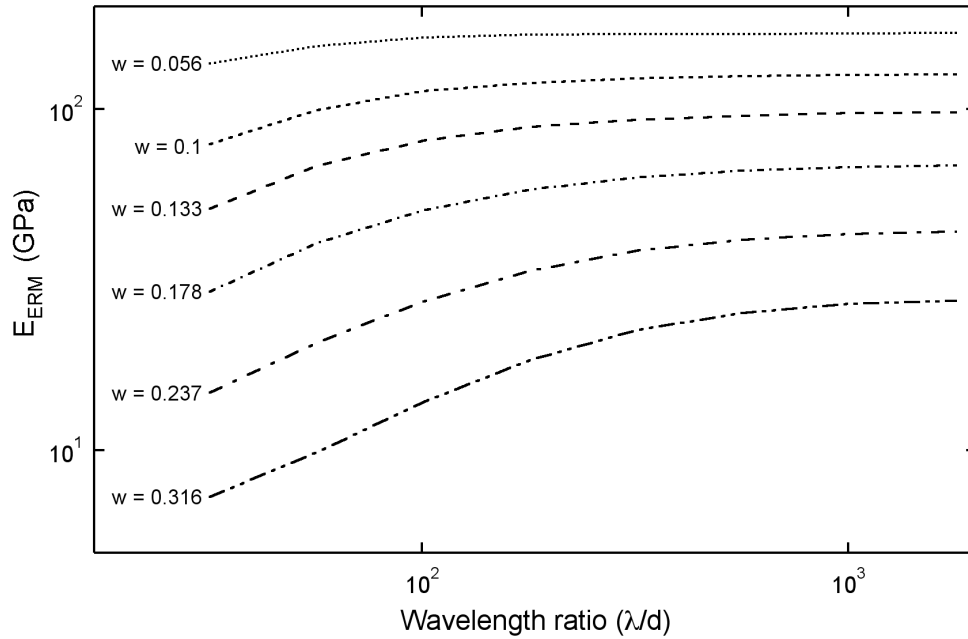


**Figure 28.  $E_{ERM}$  as a function of nanotube wavelength ratio ( $\lambda/d$ ) for different values of nanotube waviness. ( $E_{NT}=200$  GPa,  $E_{matrix}=1$  GPa).**

In Figure 29  $E_{ERM}$  (normalized with respect to  $E_{NT}$ ) is presented as a function of  $E_{ratio}$  for different values of waviness with  $\lambda/d=100$ . Note that when the phase moduli are equal ( $E_{ratio}=1$ ), the finite element cell is homogeneous and  $E_{ERM}=E_{NT}=E_{matrix}$ ; while not shown explicitly in Figure 29 all curves monotonically approach this point. With this in mind we note the strong initial decrease in  $E_{ERM}/E_{NT}$  for small values of  $E_{ratio}$ , revealing the critical role of the mechanical constraint of surrounding matrix for this case. As  $E_{ratio}$  increases the impact of the mechanical constraint diminishes, resulting in minimal changes in  $E_{ERM}/E_{NT}$  for larger values of  $E_{ratio}$  (note that in the limit as  $E_{ratio} \rightarrow \infty$  the response is that of a free-standing wavy

rod). From Figure 29 the impact of nanotube waviness on  $E_{ERM}$  is again evident; for  $w=0.056$ , the effective reinforcement provided by the wavy nanotube decreases by almost 20% for  $E_{ratio}=200$ , a modulus ratio representative of those anticipated for NRPs. For larger values of waviness the decrease in  $E_{ERM}$  is even more apparent. Note that in our simulations we are interested in the *initial* reinforcing modulus of the wavy nanotube, and do not consider the effects of nanotube straightening due to the application of an applied load.

For all previous simulations the Poisson ratios of the matrix and nanotube were assumed to be equal ( $\nu_{NT}=\nu_{matrix}=0.30$ ) to simplify the analysis. For many practical nanotube-polymer systems the difference in Poisson ratio is likely to be relatively small, with  $\nu_{NT}$  typically predicted in the range of 0.20-0.30 and  $\nu_{matrix}$  for a typical structural polymer approximately 0.25-0.40.<sup>7</sup> Simulations were conducted with constant wavy NT parameters ( $E_{ratio}=200$ ,  $\ell/d=1000$ , and  $w=0.1$ ) while varying the Poisson ratio of each phase to study the impact of the Poisson ratio mismatch on  $E_{ERM}$ . The results of this study are shown in Figure 30. We found that the value of the Poisson ratio of the nanotube is immaterial, which is not surprising considering the small volume fraction of nanotube ( $< 0.05\%$ ) modeled in the finite element cell. While the effect of  $\nu_{matrix}$  is more significant, we note that the difference in  $E_{ERM}$  is only  $\sim 5\%$

---

<sup>7</sup> The use of nanotubes as reinforcement in elastomers could potentially utilize the high elastic strains of the nanotubes (Barraza, Pompeo et al. 2002). For such polymer systems the Poisson ratios are closer to 0.5, and the Poisson ratio mismatch may be more significant.

for  $\nu_{\text{matrix}}$  between 0.25 and 0.40. Thus the results presented in this paper for  $\nu_{\text{NT}} = \nu_{\text{matrix}} = 0.30$  are in general applicable to a wide range of typical NT-polymer composite systems.

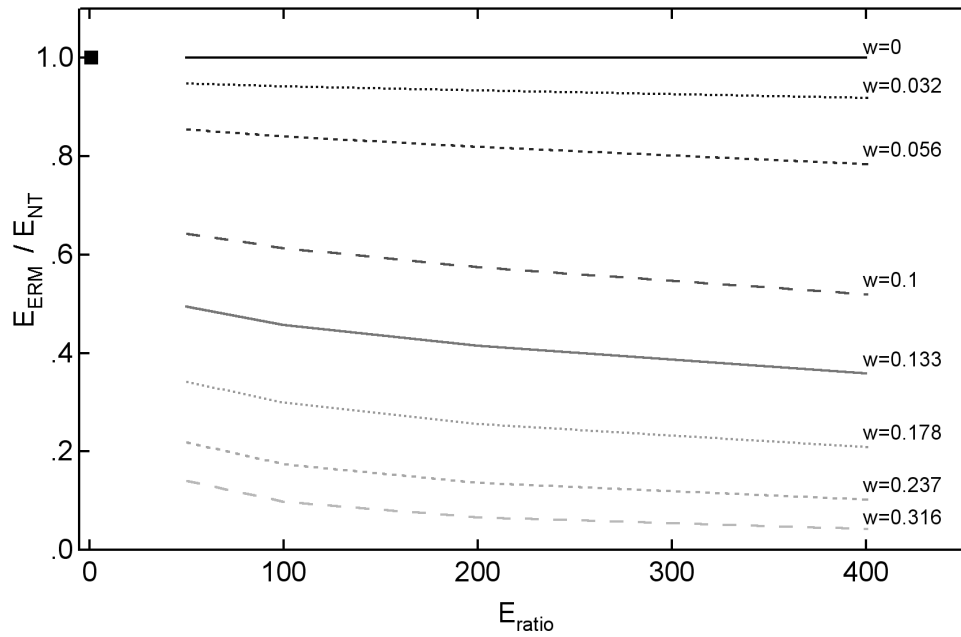


**Figure 29. Normalized  $E_{\text{ERM}}$  (with respect to  $E_{\text{NT}}$ ) as a function of  $E_{\text{ratio}}$  for  $\nu/d=100$ . For  $E_{\text{ratio}}=1$ , the material is homogeneous and  $E_{\text{ERM}}=1$  as marked; all curves monotonically approach this point (not shown for clarity).**

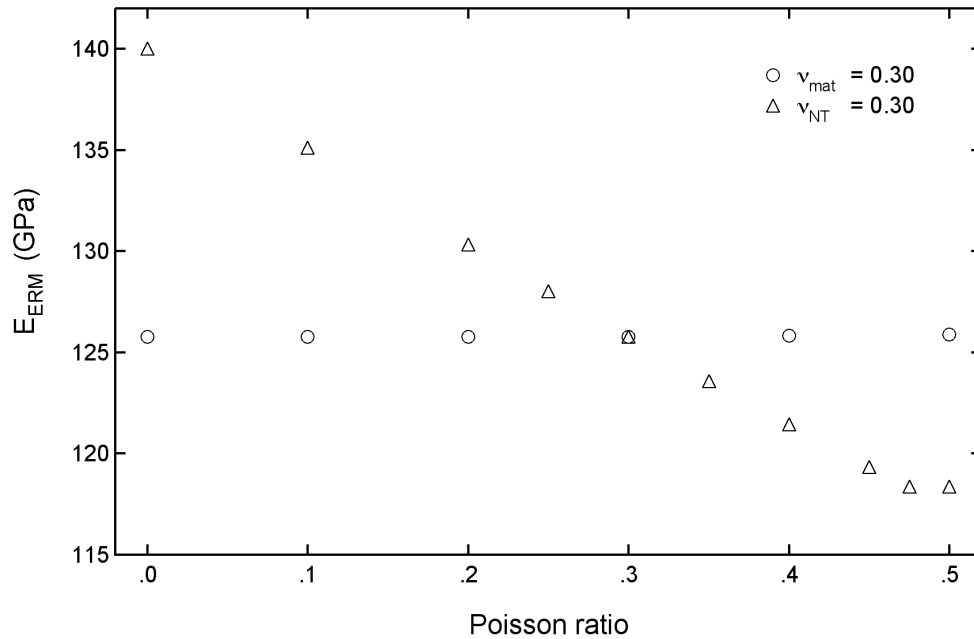


**Figure 30. Effect of Poisson ratio on the  $E_{ERM}$  values calculated from the FEM simulations. ( $\lambda/d=1000$ ,  $E_{ratio}=200$ ,  $w=0.1$ )**

In summary, we have found that the effective reinforcing modulus  $E_{ERM}$  of an embedded, wavy nanotube is strongly dependent on its geometry and the ratio of the phase moduli. As expected, the stiffening effect of the wavy nanotube decreases as the waviness of the nanotube increases, while stiffening increases as the wavelength ratio  $\lambda/d$  increases. We have also shown that  $E_{ERM}$  is a function of the ratio of the phase moduli, as the constraint of the surrounding matrix on the straightening of the wavy nanotube can be significant. Further, we have seen that for values of these parameters which are likely to be representative of wavy nanotubes embedded within a polymer

matrix, this reduction in effective modulus can be quite substantial, suggesting that the waviness of the embedded nanotubes will result in less than optimal reinforcement.

### *Analytic expressions for $E_{ERM}$ for large wavelength ratios*

From our numerical simulations we have found that for sufficiently large wavelength ratios (on the order of  $\lambda/d > 500$ , dependent on the waviness ratio), the effective reinforcing modulus  $E_{ERM}$  remains virtually constant for increasing wavelength ratios. To illustrate, Figure 31 shows how the log of  $E_{ERM}$  varies with respect to the waviness ratio for four difference ratios of phase moduli with  $\lambda/d=1000$ . Using a non-linear least squares solver we found that, for sufficiently large  $\lambda/d$ ,  $E_{ERM}$  can be approximated as

$$\log E_{ERM}(w, E_{ratio}) = \log E_{ratio} + k_1 w + k_2 w^2 + k_3 w^3. \quad (57)$$

For  $E_{ratio}=200$ , the curve fit parameters in (57) were found to be  $k_1=-0.947$ ,  $k_2=-12.90$ , and  $k_3=22.27$ . This curve fit is represented by the solid line in Figure 31, which demonstrates that the functional form of (57) well represents the data from our finite element analysis.

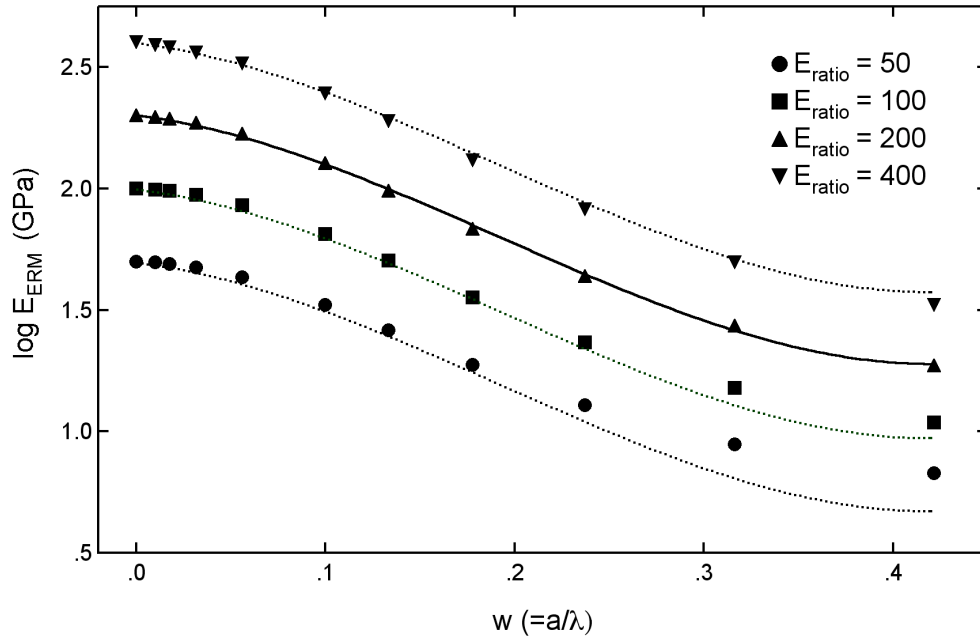


**Figure 31. Plot of  $\log E_{ERM}$  versus waviness for  $\square/d=1000$ .**

Unexpectedly, from Figure 31 it appears that the responses for different  $E_{ratio}$  seem to be related, such that the curves can be superposed (particularly for lower waviness ratios) via an appropriate vertical shifting procedure. Such a shifting procedure can be used to find the response for a particular value of  $E_{ratio}$  given the known response at a reference  $E_{ratio}$ , via

$$\log E_{ERM}(w, E_{rat}) = \log(w, E_{ERM_{ref}}) + \log\left(\frac{E_{rat}}{E_{ERM_{ref}}}\right). \quad (58)$$

This fit is demonstrated by the dashed lines in Figure 31, where the curve fit for  $E_{ratio}=200$  has been used as the reference data. This vertical shifting procedure is seen

to well describe the response for different ratios of the phase moduli, particularly for smaller waviness ratios.

We stress that the vertical shifting procedure given in (58) is only appropriate for very large values of  $\lambda/d$ , such that  $E_{ERM}$  is approximately independent of the aspect ratio. This is verified in Figure 32, which shows a plot similar to Figure 31 but for a smaller aspect ratio ( $\lambda/d=100$ ). Here it is apparent that while the general shapes of the  $E_{ERM}$  curves appear similar, the responses for different  $E_{ratio}$  cannot be related via a simple vertical shifting procedure.

While this shifting procedure is limited in that it is only applicable for larger values of the wavelength ratio  $\lambda/d$ , based on Figure 28 we note that for sufficiently small waviness ratios, the requirement of large wavelength ratio is greatly reduced. As discussed earlier, the efficiency of the nanotubes as structural reinforcement is greatly reduced for small wavelength and large waviness ratios, suggesting that NRP fabrication techniques that can control these parameters will optimize the effective modulus of nanotube-reinforced polymers. If the waviness of the embedded NTs is minimized, then the shifting procedure outlined in this section *may* be useful in analyzing  $E_{ERM}$ , and would significantly reduce the number of finite element simulations required. However, for consistency we will use  $E_{ERM}$  values calculated directly from our finite element analysis throughout the remainder of this chapter.

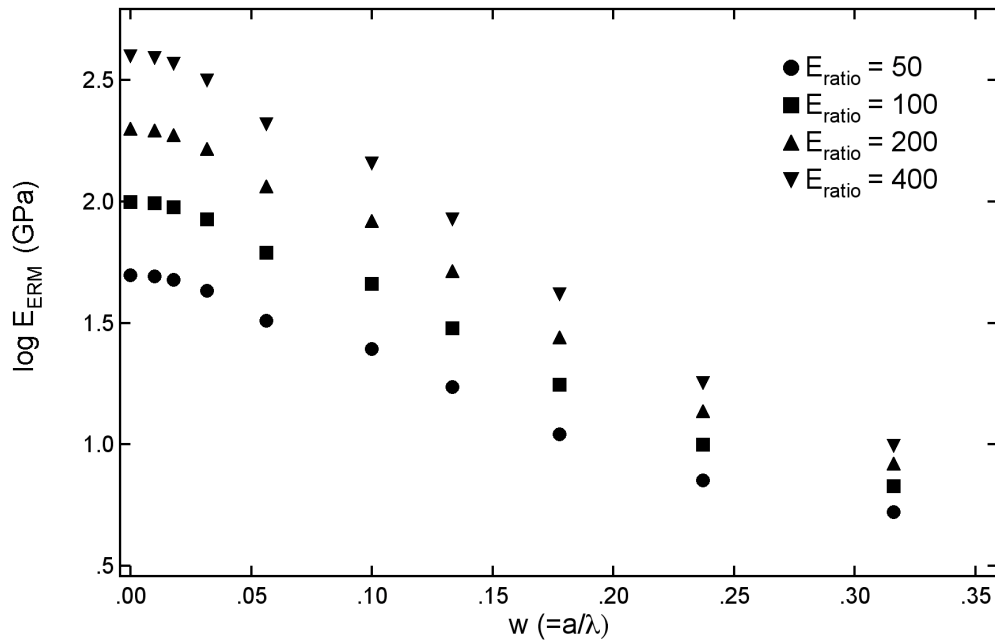
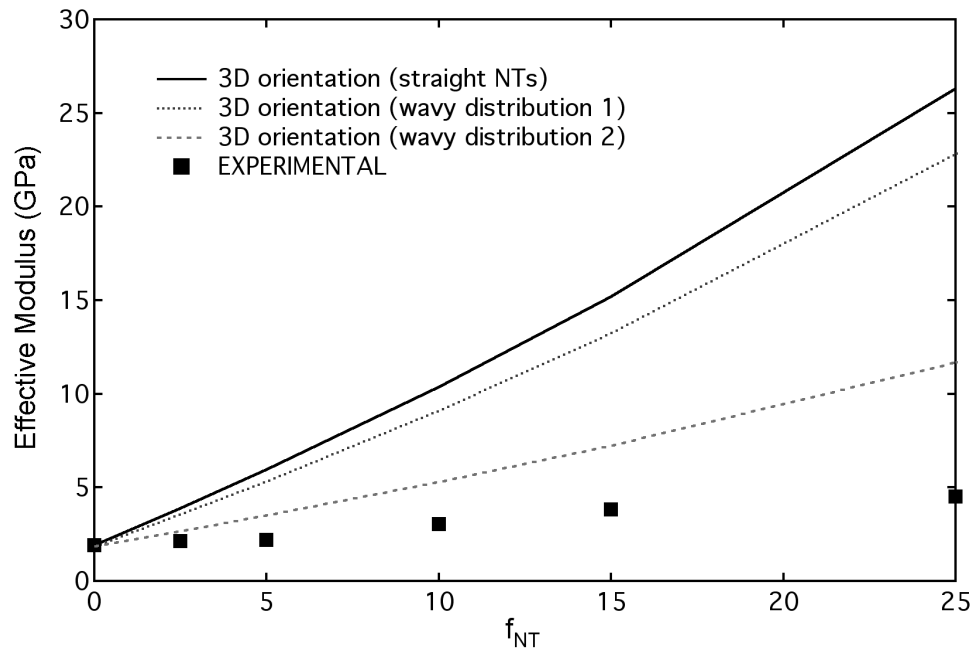


Figure 32. Plot of  $\log E_{ERM}$  versus waviness for  $l/d=100$ .

### *Micromechanical effective modulus predictions using $E_{ERM}$*

We are now in the position to use  $E_{ERM}$  within traditional micromechanics techniques in order to predict the effective modulus of NRPs. Here we highlight the procedure outlined in Figure 26 by comparing effective modulus predictions obtained using the Mori-Tanaka method with experimental tensile modulus data for various loadings of MWNTs in polystyrene (Dow 666) (Andrews, Jacques et al. 2002). The nanotubes used in this study were grown via a chemical vapor deposition process using Xylene-ferrocene (Andrews, Jacques et al. 1999) and dispersed within the polystyrene matrix via shear mixing in a Haake PolyLab bowl mixer. While the

researchers report good dispersion of the NTs within the matrix, in situ TEM straining studies have found evidence of inadequate bonding between the phases (Andrews 2001).



**Figure 33. Experimental data for MWNTs in polystyrene (Andrews, Jacques et al. 2002) and micromechanical predictions of NRP effective moduli assuming a 3D random orientation of straight and wavy nanotubes.  $E_{NT}=450$  GPa.**

In Figure 33 and Figure 34 we present the experimental data for the effective tensile modulus as a function of volume fraction of MWNTs, together with the Mori-Tanaka predictions assuming a single phase of *straight* NT inclusions randomly orientated inclusions in 3D and 2D space, respectively. Also shown are the predictions

obtained considering nanotube waviness by assuming each of the nanotube waviness distributions given in Table 7. Lacking an appropriate image of the nanostructure, these waviness distributions are loosely based on the NRP images shown in Figure 18 and represent two potential types of waviness (minimal waviness and more moderate waviness) that may be anticipated for nanotubes embedded within a polymer matrix.<sup>8</sup> For each waviness distribution  $E_{ERM}$ , for each nanotube phase was found from the finite element model described previously with  $E_{ratio}=200$  and  $\square/d=100$ . An  $E_{ratio}$  of 200 was selected to approximate a value of  $E_{NT}=450$  GPa that has been given in the literature for the modulus of NTs grown using a similar CVD method (Pan, Xie et al. 1999). These  $E_{ERM}$  values are given in Table 7. Given the waviness distribution and appropriate values of  $E_{ERM}$ , the multiphase composite analysis described in the previous section can be implemented.

---

<sup>8</sup> While it would be desirable to image a representative portion of the actual NRP sample to obtain the waviness distribution, our results nonetheless clearly demonstrate how nanotube waviness can significantly decrease the effective modulus of the NRP.

waviness ( $w=a/\lambda$ )	$E_{ERM}$ (GPa)	Volume fraction	
		NT distribution 1	NT distribution 2
0	450	0.4	0.05
0.05	383	0.4	0.15
0.1	260	0.2	0.3
0.25	57	0	0.3
0.5	10	0	0.2

**Table 7. Effective reinforcing moduli and hypothetical NT waviness distributions in the micromechanics analysis. ( $E_{ERM}$  values for  $E_{ratio}=200$  and  $\lambda/d=100$ )**

What is most striking about the results presented in Figure 33 and Figure 34 are the large discrepancies between the Mori-Tanaka predictions assuming *straight* nanotubes and the experimentally measured moduli. While the experimental modulus has been significantly enhanced with the addition of the NTs (the modulus increases by a factor of two for 15 vol% NTs), the realized improvements in modulus are significantly less than the micromechanics predictions with straight nanotubes would indicate. Integrating moderate nanotube waviness (NT distribution 2) into the effective moduli predictions is shown to drastically decrease the moduli predictions, suggesting that NT waviness may be one factor limiting the modulus enhancement of NRPs.

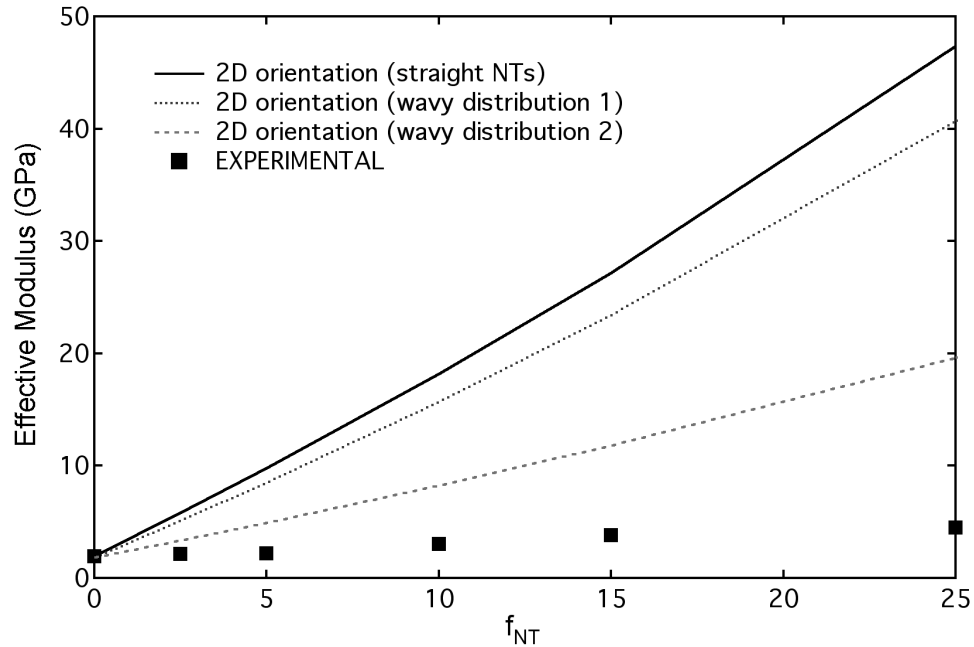


**Figure 34. Experimental data for MWNTs in polystyrene (Andrews, Jacques et al. 2002) and micromechanical predictions of NRP effective moduli assuming a 2D random orientation of straight and wavy nanotubes.  $E_{NT}=450$  GPa.**

Similar results were found for other NRP experimental data presented in the literature. Figure 35 shows the experimental modulus and micromechanics predictions obtained for 5 wt% MWNTs embedded in epoxy (Schadler, Giannaris et al. 1998), using the second waviness distribution and corresponding  $E_{ERM}$  values found in Table 7. Again the results show that the micromechanics predictions assuming straight NTs overestimate the experimental data. However, moderate NT waviness can reduce the predicted effective modulus of the NRP significantly, bringing the predictions more in line with the experimental data. The results for unidirectionally aligned NTs, also

shown in Figure 35, suggest that an order of magnitude increase in modulus may be possible for such systems.

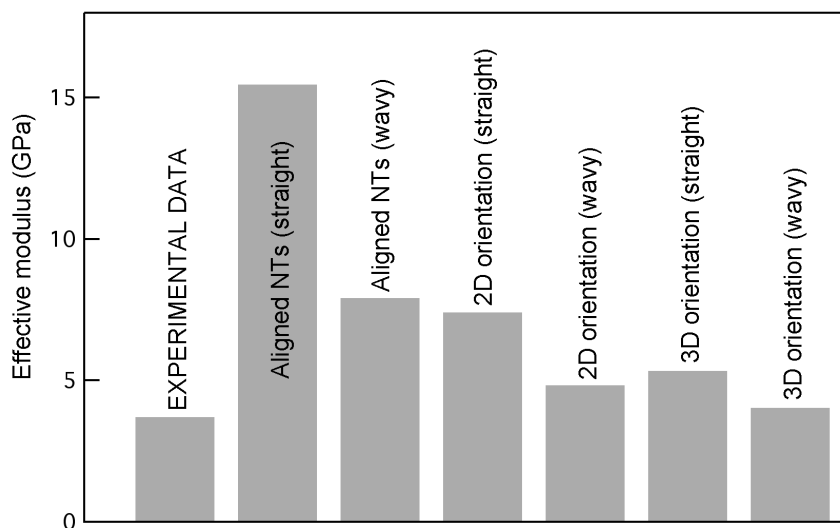


**Figure 35. Experimental data for 5 wt% MWNTs in epoxy (Schadler, Giannaris et al. 1998) and micromechanical predictions of NRP effective moduli assuming straight and wavy nanotubes with different NT orientations.**

At the moment it is impossible to distinguish the effects of nanotube waviness from other mechanisms that would tend to decrease the effective properties of the nanotube-reinforced polymer. Other conditions, such as a poor NT-polymer interface, inadequate NT dispersion, and nanotube degradation due to processing of the NRP would also result in experimental moduli less than those predicted using micromechanics. However, based on images of nanotubes embedded in polymers and

our modeling results presented here, we have demonstrated that nanotube waviness may be an additional mechanism which can strongly influence the effectiveness of nanotubes as structural reinforcement.

## **An Alternative Model to Incorporate Nanotube Waviness into Effective Moduli Predictions**

During the development of the  $E_{ERM}$  model, an alternative (albeit related) solution was conceived to incorporate inclusion waviness into micromechanical predictions of effective stiffness. In this alternative model, which we call the Numerical Strain Concentration Tensor (NSCT) method, the complete dilute strain concentration tensor  $A_r^{dil}$  is found via the solution of six separate finite element models with appropriate boundary conditions, a procedure that is described in detail in the literature (Bradshaw, Fisher et al. 2002). Once the dilute strain concentration tensor  $A_r^{dil}$  has been determined, it can then be used directly in the Mori-Tanaka solution (see equation (35)) to predict the NRP effective modulus.

The major difference between these two models is that the ERM model solves a single finite element model, analogous to a numerical tensile test, and then treats the wavy nanotube as an isotropic inclusion with a reduced modulus  $E_{ERM}$ . For the NSCT model, the solution to the six independent finite element models (with identical

geometry) yields an orthogonal effective response such that the isotropic simplification used in the ERM model is unnecessary. To demonstrate the difference in the two models, the effective moduli predictions for a two-phase *unidirectional* composite with a 10% volume fraction of NTs with  $E_{\text{ratio}}=400$  and  $\lambda/d=100$  are shown in Figure 36-Figure 38.

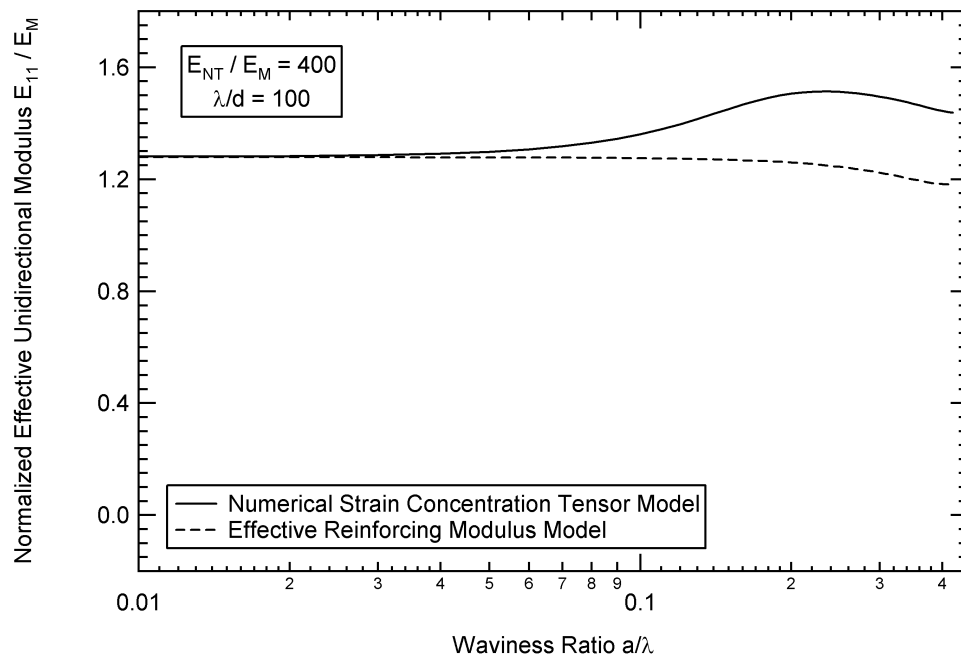


**Figure 36. Effective composite modulus  $E_{11}$  (in the x direction of Figure 21, out-of-plane of NT waviness) with increasing waviness ratio ( $a/\lambda$ ) for the ERM and NSCT models. (Bradshaw, Fisher et al. 2002)**

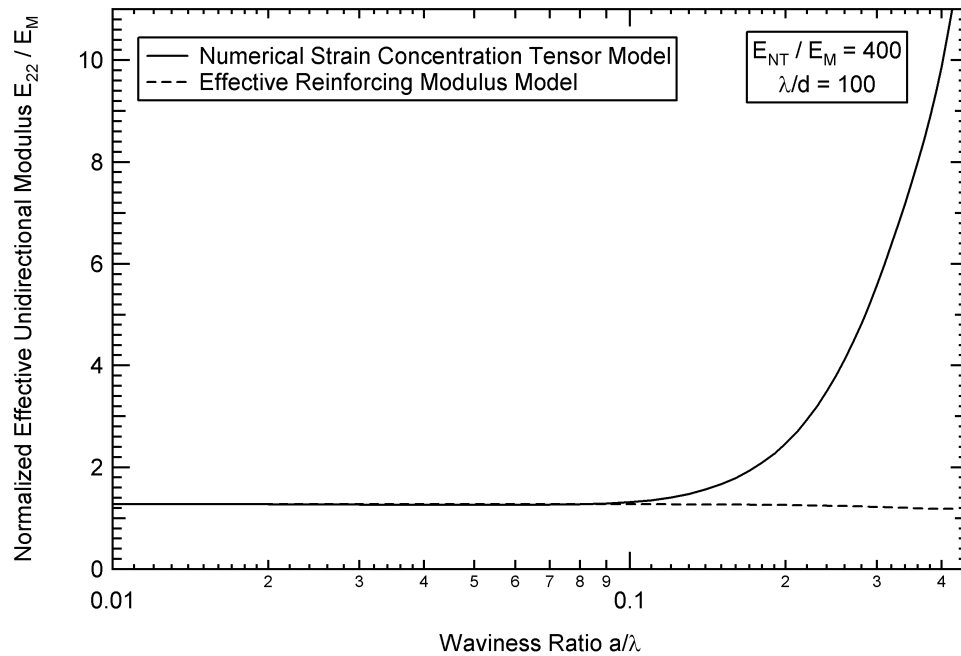


**Figure 37. Effective composite modulus  $E_{22}$  (in the y direction of Figure 21, in the plane of waviness and transverse to the NT axis) with increasing waviness ratio ( $a/\lambda$ ) for the ERM and NSCT models. (Bradshaw, Fisher et al. 2002)**

As one might expect, the largest difference between the two models is found in the  $E_{22}$  term, which the NSCT model predicts will increase for large values of waviness. This is sensible physically; as the waviness increases, the portion of the wavy nanotube that is aligned towards the 2-direction increases, such that the NT begins to provide significant reinforcement in this direction. This behavior cannot be captured in the ERM model, where only the response of a single finite element cell subject to loading parallel to the NT long axis is analyzed.

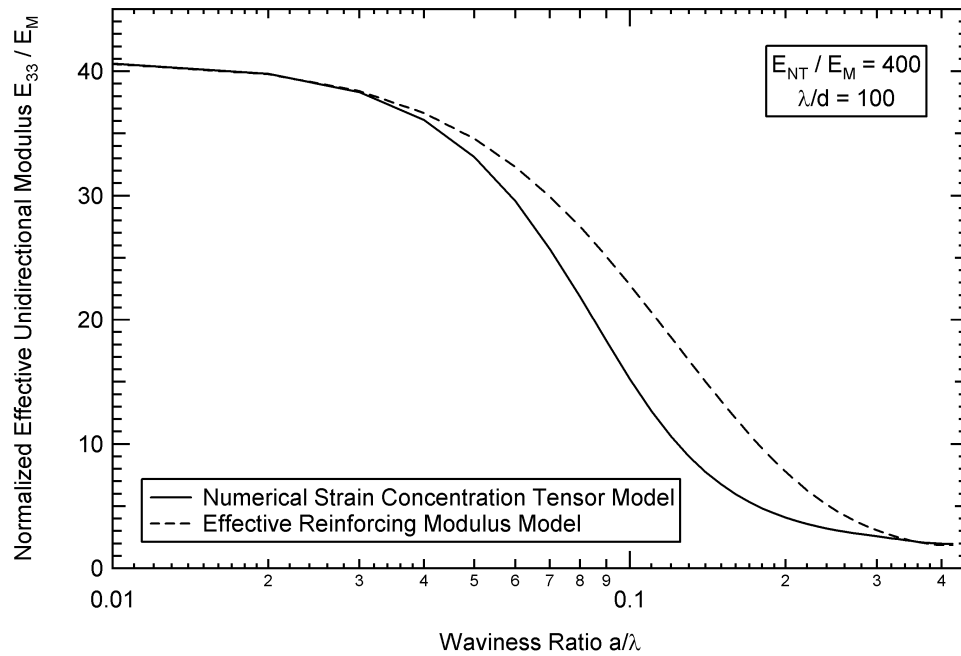


**Figure 38. Effective composite modulus  $E_{33}$  (in the z direction of Figure 21, parallel to the NT axis) with increasing waviness ratio ( $a/\lambda$ ) for the ERM and NSCT models. (Bradshaw, Fisher et al. 2002)**

The ERM and NSCT predictions for a two-phase NRP with a 3D random orientation of wavy nanotubes are shown in Figure 39. Here we assume isotropic constituent phases, a 10% NT volume fraction (where all NTs have the same waviness), and  $E_{\text{ratio}}=400$ . We see that for shorter wavelength ratios ( $\lambda/d=10$ ), the difference between the models is minimal until very large values of the waviness ratio  $a/\lambda$  are considered, at which point the NSCT model predicts a stiffer effective response. For larger wavelength ratios ( $\lambda/d=100$ ), the difference between the two models is more significant, although it should be noted that this difference is

exaggerated here given the large NT volume fraction modeled. We also note that Figure 39 assumes that all of the nanotubes have identical values of  $a/\lambda$ . As discussed previously, there is likely to be a distribution of NT waviness within the material, such that only a fraction of the nanotubes would be characterized by  $a/\lambda$  and  $\lambda/d$  parameters for which the difference between the ERM and NSCT results is significant.

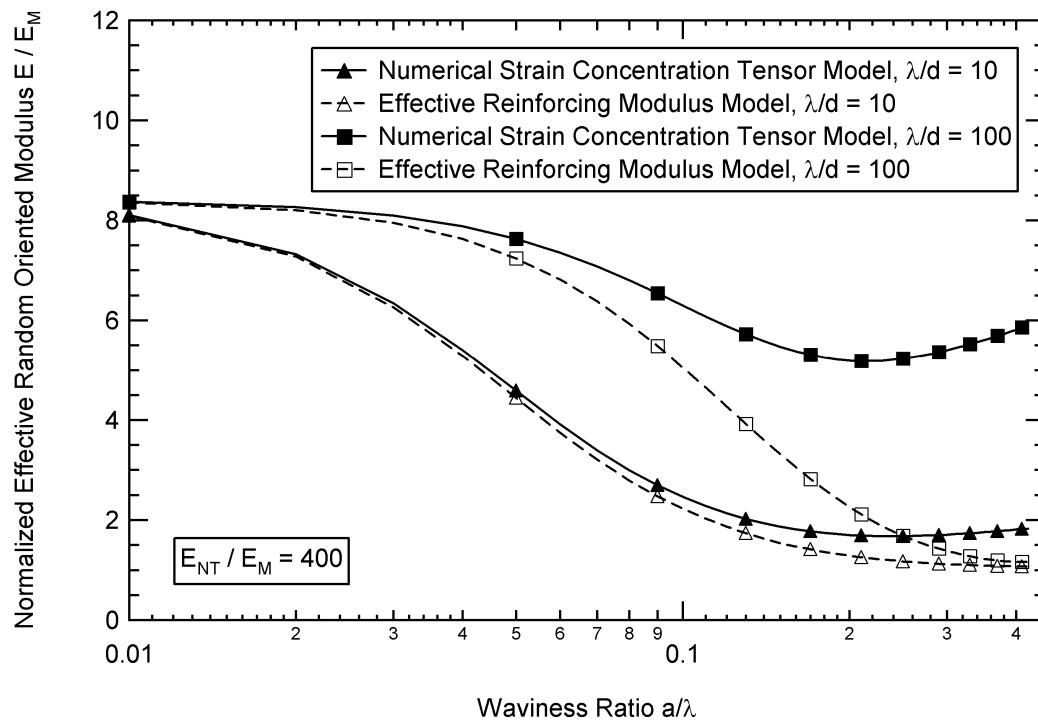


**Figure 39. Young's modulus predictions for an NRP with 3D randomly oriented wavy NTs using the ERM and the NSCT models for  $E_{ratio}=400$ . (Bradshaw, Fisher et al. 2002)**

For NRP samples with moderate waviness, the differences in moduli predictions given by the two models may be minimal and likely masked by other factors; in this case the ERM model may be preferable due to its simplicity. For cases where significant nanotube waviness is expected or has been observed, the NSCT model is preferred because it more accurately models the full impact of the wavy nanotube on the effective moduli of the NRP.

## Summary

Motivated by micrographs showing that nanotubes embedded within polymers often exhibit significant curvature, we have developed a model that incorporates this curvature into traditional micromechanical methods via a multiphase composite approach. Finite element results of embedded wavy inclusions show that the effective reinforcing moduli  $E_{ERM}$  of the inclusions quickly decreases as a function of inclusion waviness, and is also dependent on the wavelength ratio and the ratio of the phase moduli. Using material properties representative of nanotube-reinforced composites, we have shown that nanotube waviness can reduce the predicted effective moduli of these materials by a factor of two or more, and may be one reason why the modulus enhancement of NRPs, while significant, is somewhat less than predicted using standard micromechanical techniques. While for some applications (such as impact

resistance and energy absorption) nanotube waviness may be beneficial, for structural applications inclusion waviness can significantly degrade the modulus enhancement provided by the nanotube inclusions.

While here we use  $E_{ERM}$  values based on finite element modeling, alternative means to determine an appropriate value of  $E_{ERM}$ , incorporating more detailed atomic scale information, could also be used in a similar analysis. Adaptations of the current model to include inter-layer (MWNTs) and inter-tube (NT bundles) sliding, and a transversely isotropic NT inclusion, will also be addressed in future work.

Our results suggest that methods of NRP fabrication that reduce the waviness of embedded NTs would result in more efficient structural reinforcement. For example, one can hypothesize that nanotube waviness may be one reason why NRP modulus enhancement has sometimes only been reported at higher temperatures as shown in Figure 40 (Shaffer and Windle 1999; Jin, Pramoda et al. 2001). If compressive stresses developed during polymer cure introduce bending (and hence curvature) into the embedded nanotubes, significant NT reinforcement may only be realized as the NTs straighten due to polymer softening at elevated temperatures.

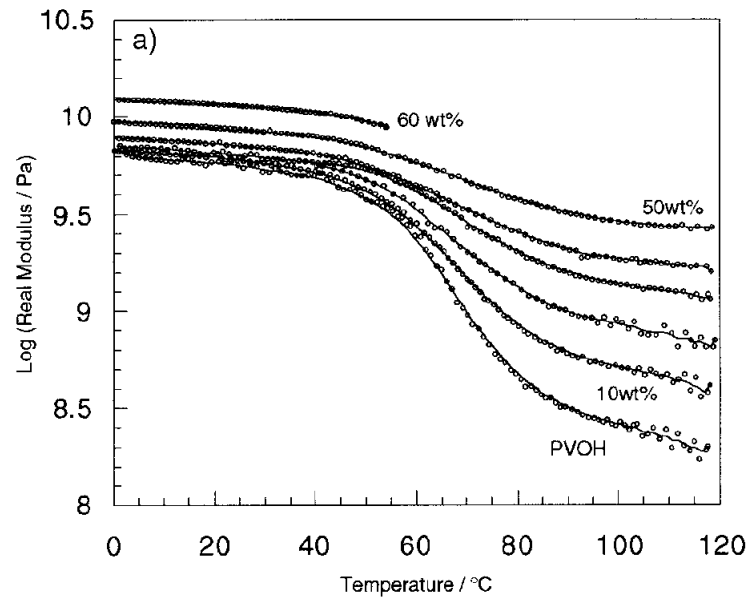


**Figure 40. Storage moduli of PVOH reinforced with MWNTs (Shaffer and Windle 1999).**

While it might seem intuitive that NT waviness would decrease the NRP effective modulus, the utility of the models presented in this Chapter is that for the first time we are able to quantify the impact of this waviness on the NRP effective modulus. One drawback of the model is that presently it is impossible to differentiate nanotube waviness from other reinforcement-limiting mechanisms in the system. Another simplification is the assumption of the sinusoidal shape describing the nanotube waviness. Based on images of free-standing and embedded nanotubes, it is likely that the waviness of the nanotube will vary both along, and between, the embedded nanotubes. Nanotube waviness is also likely to be strongly dependent on

the processing conditions and NT-polymer interaction for a particular system under investigation.

A potential means of experimentally validating the proposed model of nanotube waviness is the use of silicon nanostructures of well-defined shape and dimension, as shown in Figure 41 (Yin, Gates et al. 2000). These pieces are fabricated using a technique that combines near-field optical lithography, followed by a reactive ion etch and subsequent lift-off from the substrate. The result of the processing technique is nanometer-sized structures of single crystal silicon. This method has been proposed as a quick and efficient means of creating accurately dimensioned nanostructures at a very reasonable price.

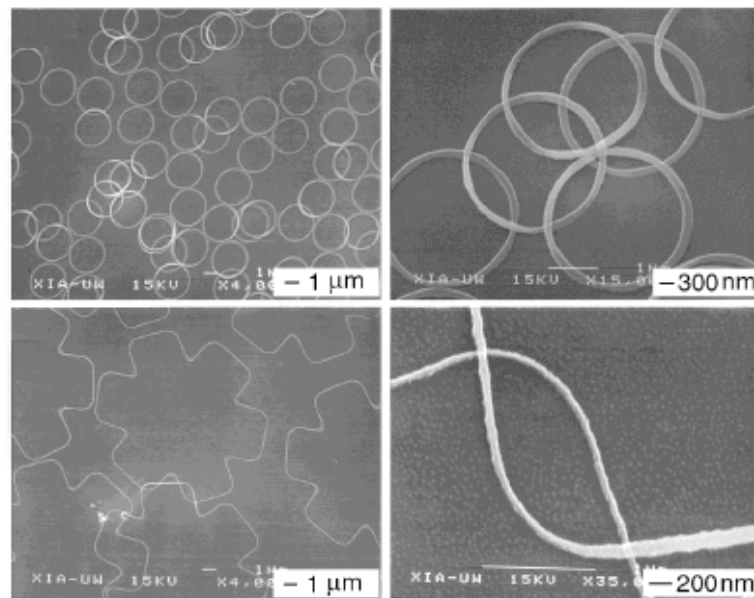


**Figure 41. SEM images of silicon nanostructures. (Yin, Gates et al. 2000)**

While the primary interest in these silicon nanostructures comes from the area of microelectronics, in regards to the current work these structures may provide model wavy inclusions of well-defined geometry as a means to experimentally validate the models proposed in this Chapter. Given that such nanowires can be easily fabricated, a model polymer matrix composite with idealized nanostructured inclusions could be produced. It would be useful to compare the experimental moduli obtained for such materials with the theoretical models presented here. While experimental validation of the proposed wavy nanotube model was beyond the scope of the work in this dissertation, future experimental work along these lines is warranted.